



Publication Year	2015
Acceptance in OA	2020-06-10T09:00:13Z
Title	Topside of the martian ionosphere near the terminator: Variations with season and solar zenith angle and implications for the origin of the transient layers
Authors	Zhang, Zhenfei, OROSEI, ROBERTO, Huang, Qian, Zhang, Jie
Publisher's version (DOI)	10.1016/j.icarus.2014.09.036
Handle	http://hdl.handle.net/20.500.12386/25980
Journal	ICARUS
Volume	251

Accepted Manuscript

Topside of the Martian Ionosphere near the Terminator: Variations with Season and Solar Zenith Angle and Implications for the Origin of the Transient Layers

Zhenfei Zhang, Roberto Orosei, Qian Huang, Jie Zhang

PII: S0019-1035(14)00511-9

DOI: <http://dx.doi.org/10.1016/j.icarus.2014.09.036>

Reference: YICAR 11283

To appear in: *Icarus*

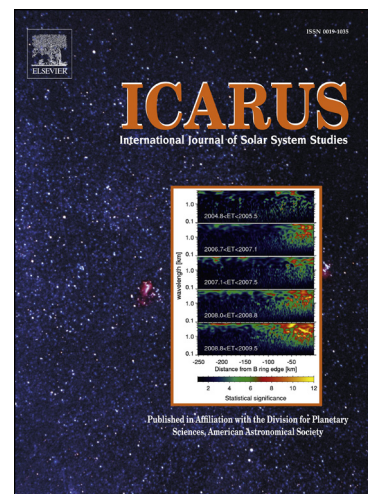
Received Date: 17 September 2013

Revised Date: 6 July 2014

Accepted Date: 22 September 2014

Please cite this article as: Zhang, Z., Orosei, R., Huang, Q., Zhang, J., Topside of the Martian Ionosphere near the Terminator: Variations with Season and Solar Zenith Angle and Implications for the Origin of the Transient Layers, *Icarus* (2014), doi: <http://dx.doi.org/10.1016/j.icarus.2014.09.036>

This is a PDF file of an unedited manuscript that has been accepted for publication. As a service to our customers we are providing this early version of the manuscript. The manuscript will undergo copyediting, typesetting, and review of the resulting proof before it is published in its final form. Please note that during the production process errors may be discovered which could affect the content, and all legal disclaimers that apply to the journal pertain.



**Topside of the Martian Ionosphere near the Terminator: Variations
with Season and Solar Zenith Angle and Implications for the Origin
of the Transient Layers**

Zhenfei Zhang^{a,*} Roberto Orosei^b Qian Huang^c Jie Zhang^a

^a Institute of Mathematical Geology and Remote Sensing, China University of Geosciences
(Wuhan), 388 Lumo Rd., 430074 Wuhan, China

Email:

Zhenfei Zhang: zfzhang@cug.edu.cn

Jie Zhang: zhangjie0130@126.com

^b Istituto di Radioastronomia, Istituto Nazionale di Astrofisica, Via Piero Gobetti, 101
I-40129, Bologna, Italy

Email:

Roberto Orosei: roberto.oroisei@inaf.it

^c Institute of Planetary Science, China University of Geosciences (Wuhan), 388 Lumo
Rd., 430074 Wuhan, China



Email:

Qian Huang: huangqian@shao.ac.cn

* Corresponding author.

Abstract

In this paper, the morphological variations of the M2 layer of the Martian ionosphere with the Martian seasons and solar zenith angle (SZA) at the terminator are investigated. The data used are the MARSIS (Mars Advanced Radar for Subsurface and Ionosphere Sounding) measurements (approximately 5,000 ionograms) that were acquired from 2005 to 2012, which have a $SZA \geq 85^\circ$ and detect the topside transient layers. A simple, effective data inversion method is developed for the situation in which the upper portion of the height profile is non-monotonic and the observed data are insufficient for adequate reduction. The inverted parameters are subsequently explored using a statistical approach. The results reveal that the main body of the M2 layer (approximately 10 km below the first topside layer) can be well-characterized as a Chapman layer near the terminator ($SZA = 85^\circ - 98^\circ$), notwithstanding the high SZA and the presence of the topside layers. The height of the first topside layer tends to be concentrated approximately 60 km (with a standard deviation of ~ 20 km) above the main density peak. The peak density and height of the first topside layer are positively correlated to the density and height of the main peak, respectively. The density and height of the first topside layer appear to be independent of the SZA, but possess seasonal variations that are similar to those of the main layer. The height of the topside layer is greater (by ~ 10 km on average) in the southern spring and summer than in the southern autumn and winter, coinciding with the observation that, in the southern spring and summer, the underlying atmosphere is warmer due to dust heating [e.g., Smith, 2004. Interannual variability in TES atmospheric observations of Mars during 1999–2003. *Icarus* 167, 148–165]). The statistical regularities of the parameters suggest a possibility that the formation of the topside layers are closely related to the processes of photoionization and diffusion that occur on the topside of the M2 layer. We propose that development of beam-plasma instabilities in the transitional region (between the lower Chapman region and the upper transport-dominating region) is possibly a mechanism that is responsible for the occurrences of the topside layers.

Keywords: Mars; Ionosphere; Terminator; MARSIS; Plasma

ACCEPTED MANUSCRIPT

1. Introduction

Characterization of the Martian ionosphere has been greatly promoted since 2005 when measurements by the Mars Advanced Radar for Subsurface and Ionosphere Sounding (MARSIS) on board the ESA mission Mars Express (MEX) [Picardi *et al.*, 2004], became available. Based on MARSIS data, extensive investigations have been conducted by many researchers to characterize the daytime [e.g., Gurnett, *et al.*, 2005; Gurnett *et al.*, 2008; Morgan *et al.*, 2008; Kopf *et al.*, 2008; Nielsen *et al.*, 2007a; Nielsen *et al.*, 2007b; Akalin *et al.*, 2010; Němec *et al.*, 2011] and nighttime [Safaeinili *et al.*, 2007; Gurnett *et al.*, 2008; Němec *et al.*, 2010] ionosphere of Mars. Current knowledge of the main ionospheric layer of Mars (called M2) that have been achieved by using observations from various instruments, including MARSIS, can be found in a review by Withers [2009].

Previous studies indicate that the daytime M2 layer is well approximated by the Chapman model, which represents a photoionization and dissociative recombination quasi-equilibrium mechanism that is controlled mainly by the solar zenith angle (SZA) [e.g., Gurnett, *et al.*, 2005; Gurnett *et al.*, 2008; Morgan *et al.*, 2008; Němec *et al.*, 2011]. Beside the SZA, many factors affect the Martian ionosphere to various degrees. For example, seasonal atmospheric actions (e.g., [Zou *et al.* 2005; Morgan *et al.* 2008]), the crustal magnetic field (e.g., [Krymskii *et al.*, 2003; Lillis *et al.*, 2008]), the Martian longitude (related to tides in the atmosphere that influence the ionosphere) [e.g., Bougher *et al.*, 2004; Breus *et al.*, 2004], the Martian ground surface topography (related to wind patterns on Mars [Wang and Nielsen, 2004]), Mars rotation [Shinagawa, 2000], solar rotation (related to periods of relatively high and low solar fluxes) [Withers and Mendillo, 2005], distance from Mars to the Sun (related to the strength of solar radiation [e.g., Breus *et al.*, 2004; Morgan *et al.*, 2008; Němec *et al.* 2011]), and the solar wind (induces magnetic fields and interacts with the topside of the ionosphere) [e.g., Wang and Nielsen, 2003a; Kopf *et al.*, 2008; Dubinin *et al.*, 2008]. Near the terminator, the ionosphere has a sparser plasma density, higher altitude and stronger variability in the profile shape than the ionosphere far from the terminator in the daytime (e.g., [Gurnett, *et al.*, 2005; Gurnett *et al.*, 2008; Morgan *et al.*, 2008; Withers, 2009; Němec *et al.*, 2011]). The nighttime Martian ionosphere is characterized as patchy and more variable in

density; it is formed mainly by plasma transport from the daytime, as well as by energetic electron precipitation where open magnetic field lines of crustal magnetic anomalies exist [Fox and Bzannon, 1993; Safaeinili et al., 2007; Withers, 2009; Lillis et al., 2009; Fillingim et al., 2010; Němec et al., 2010]. The nighttime ionosphere is much less frequently detected by MARSIS as compared to its daytime counterpart (the occurrence rate of ionospheric reflections in the nighttime MARSIS data records is <20% at $SZA=100^\circ$ and <5% at $SZA=125^\circ$) [Němec et al. 2010].

A second layer above the main density peak is often detected by MARSIS throughout the daytime, as was reported by several groups [Gurnett, et al. 2008; Kopf et al., 2008; Wang et al., 2009]. The second layer is characterized as transient, variable in density ($2.0e+10$ to $7.0e+10 \text{ m}^{-3}$) and altitude (180 – 220 km), and has a decreasing occurrence rate with increasing SZA (from approximately 60% near the sub-solar point to less than 5% near the terminator) [Kopf et al., 2008]. A third layer can also be observed in the MARSIS data, but it is rare (~1%) [Kopf et al., 2008]. No clear relationships are found between the layers and surface features, the crustal magnetic fields, variations in the solar EUV radiation and solar energetic particle events [Kopf et al., 2008]. The origin of the transient layers is not well understood. Gurnett, et al. [2005] and Kopf et al. [2008] suggest that the layers might result from the velocity shear between the solar wind and the main layer ionosphere, which may generate non-linear structures, such as curl-over or detached plasma clouds, due to Kelvin-Helmholtz instability. However, the reason that the occurrence rate of the layers decreases toward the terminator (where the velocity shear is expected to be stronger) remains unclear [Kopf et al., 2008].

In this paper, we investigate the upper portion of the M2 layer near the terminator using the MARSIS Active Ionosphere Sounding mode (AIS) measurements. “Upper portion” refers to the altitude where the topside transient layers are detected. Hereafter, we call a topside transient layer a “top layer”. Our goal is to examine how plasma density changes in this region with Martian seasons and SZA and if and how these changes are related to the variations of the main density peak. This may provide more constraints on the origin of the transient layers in the near-terminator region, and it may also provide information on the daytime ionosphere transition into the nighttime ionosphere. A simple, effective method for

data inversion is developed to retrieve the relevant ionospheric parameters. The inverted parameters are investigated by a statistical approach. In the remainder of the paper, we shall specifically describe the data (Sec. 2), method (Sec. 3) and results (Sec. 4). A discussion (Sec. 5) and conclusions (Sec. 6) are subsequently presented.

2. Data

2.1. MARSIS Radar Parameters and Observations

The MARSIS instrument and techniques are introduced by several authors [e.g., *Picardi et al.*, 2004; *Gurnett, et al.*, 2005; *Jordan et al.*, 2009; *Morgan et al.*, 2013]. Nevertheless, we shall briefly describe the radar parameters and data records of the MARSIS radar in the AIS mode for ease of reference. In the AIS mode, MARSIS transmits pulses at 160 quasi-logarithmically spaced sounding frequencies between 0.1–5.5 MHz. The pulses have a 10.9 kHz bandwidth and 91.3 μ s duration. The receiving time window extends from 0.1625 ms to 7.57 ms after transmission and is divided into 80 contiguous time bins of 91.3 μ s each. The received signals are recorded as power intensities ($V^2 m^{-2} Hz^{-1}$). The transmission – receiving cycle is repeated in ascending order of the center frequencies. A complete scan of the 160 frequencies (a sweep cycle) takes 1.26 s. The sweep cycle is repeated once every 7.35 s. The recorded data of a sweep cycle is called a frame, which can be displayed with an ionogram (i.e., a plot of echo intensity as a function of time delay and frequency). Contiguous frames on an orbit of MEX are organized into a data file. Along with the science data files, a geometrical data file records information of spacecraft position, velocity, SZA, solar longitude, and so on, for each frame. During the AIS mode, the spacecraft altitude changes between approximately 1200 km and 260 km.

2.2. Data Selection

To study the Martian ionosphere using MARSIS data, vertical reflections must be recognized in the ionograms. The ionograms are usually noisy as the vertical echoes may be disturbed by oblique echoes, electron plasma oscillation harmonics, electron cyclotron echoes, interference of echoes from different regions and other noise. In many cases, the vertical echo

trace is unclear or segmented [e.g., *Gurnett et al.*, 2008; *Kopf et al.*, 2008]. At the low sounding frequencies, the vertical echoes are often undetected due to weak reflections [e.g., *Wang et al.*, 2009] and are usually more disturbed than those at higher frequencies. The noise and/or defective echo traces prevent the retrieval of appropriate signals, and data should be selected.

Because we are interested in the upper portion of the ionosphere near the terminator when transient layers are detected, we choose MARSIS data with a SZA $\geq 85^\circ$ that reveal such layers. The existence of a layer is indicated by the presence of a “cusp” (or ledge or step) on the ionospheric echo trace in an ionogram. A cusp refers to the phenomenon in which the echo trace bends steeply toward the direction of the increasing time delay. A cusp develops when the sounding wave frequency approaches the plasma frequency, whereby the refractive index drops below one and the round-trip travel time for the wave increases [*Gurnett, et al.* 2008; *Kopf et al.*, 2008; *Wang et al.*, 2009]. A cusp occurs at the high frequency end of the ionospheric echo trace, which indicates the peak plasma frequency of the main layer. We call this the first cusp. If an extra layer exists on the topside of the main layer, a second cusp may be observed at a lower frequency position on the echo trace, which indicates the peak plasma density of this topside layer. In the MARSIS ionograms, the first cusp is usually discernable, but a second cusp is much less frequent. We select ionograms that fit the following three requirements, besides the SZA ($\geq 85^\circ$) condition:

(1) The first cusp is discernable. This ensures that the maximum reflection frequency of the main plasma layer can be extracted.

(2) A second cusp is discernable, or the trace bends steeply towards the direction of the increasing time delay at the lower frequency end, which indicates that an unseen cusp is close to this end. This criterion ensures the presence of a top layer with an extractable peak density.

(3) Between the lower and higher frequency ends, the trace is continuous. This means that the density profile segment represented by the trace can be described by a continuous function of altitude.

We examined all of the calibrated, reduced data record (RDR) files of MARSIS AIS mode that are publicly available before the end of 2012. The result was 3793 files (orbit numbers from 1848 to 9879) that contain 656,767 frames, among which 262,756 have a

$SZA \geq 85^\circ$. Using the three outlined criteria, we selected 4988 frames in total (scattered in 621 MEX orbits) for further analysis. Approximately 97% of the frames that satisfy the SZA condition are excluded by criterion (2), and ~1% of the frames were excluded by criteria (1) and (3). The selected frames constitute a fraction of $4988/262,756=1.86\%$. All of the selected data are associated with a spacecraft altitude >300 km; at low spacecraft altitudes, the ionograms tend to be more disturbed by the local electron plasma oscillation harmonics. The spatial distribution of the selected frames is shown in Fig. 1. The selected data are relatively sparse at low latitudes. This is mainly due to the high SZA condition (the SZA tends to be larger at higher latitudes than in the near-equator regions). In Fig. 1, more data points are present in the Northern Hemisphere than in the Southern Hemisphere, where the ionograms tend to be noisier due to the disturbance of the electron cyclotron echoes. The selected data have a $SZA < 98^\circ$ with few exceptions, which emphasized the fact that distinct vertical ionospheric echoes are rare in the MARSIS ionograms at large SZAs ($>98^\circ$) [Němec *et al.* 2010].

2. 3. Data Extraction

Data extraction is used to retrieve data points (echo time delays and their corresponding wave frequencies) from each of the selected ionograms. We extract data points visually from the vertical echo trace on the computer screen. Only 6 points are extracted for each ionogram and are sufficient for our inversion method (Sec. 3.2.3). Of the 6 points, one is at the first cusp, one is at (or close to) the second cusp, and the remaining 4 are in between. Figure 2 shows an example of the selected ionograms, the data selection criteria and the extracted data points. Also shown in Fig. 2 is a simulated vertical echo trace based on the data inversion, which we will describe in Sec. 3.2.

3. Inversion

3.1. Existing Inversion Methods

An inversion is used to retrieve the real electron density profile parameters from the ionograms. Three types of inversion methods are common [Titheridge, 1998]: (1) The

lamination method, which calculates the profile points step by step beginning from the lowest frequency. Each step begins from the last calculated real height and is determined to fit the next time delay measurement. (2) The single polynomial method, which uses a single mathematical expression to represent the entire profile. (3) The overlapping polynomial method, which separates the entire profile into more than one overlapped frequency range and uses high order polynomials to fit each of the ranges. Using MARSIS data, several authors have developed lamination methods to invert density profiles of the daytime [e.g., *Nielsen et al.*, 2006; *Morgan et al.*, 2008; *Morgan et al.*, 2013] or nighttime [*Němec et al.*, 2010] ionosphere. These lamination methods require two assumptions. First, the profile above the main density peak is monotone-decreasing upward. An exponential function is usually adopted (e.g., [*Morgan et al.*, 2008]). Second, the real height of the reflection point that corresponds to the lowest sounding frequency is known. This height can often be inferred by interpolation if the electron density near the spacecraft is known [e.g., *Morgan et al.*, 2013]. By measuring the in situ electron plasma oscillation harmonics, an in situ electron density can be obtained if the spacecraft altitude is lower than ~700 km [*Duru et al.*, 2008; *Duru et al.*, 2010]. If an in situ density is not attainable, then it may be reasonably estimated [e.g., *Nielsen et al.*, 2006].

In the situations where one or two top layers are present, *Kopf et al.* [2008] suggest that the density profile for each top layer can be approximated by a Gaussian form. *Kopf et al.* [2008] note that the presence of the top layers leads to indeterminacy in the inversion process. Therefore, they assume the total density profile is monotonic across the interfaces between the layers. The method used was not described any further in [*Kopf et al.*, 2008].

3.2. Plasma Density Profile Model

Our inversion method is based on a “simplified” profile model. Here, we first introduce a “normal” model and discuss why and how it is simplified.

3.2.1. A Quantitative Profile Model

We assume the profile of a top layer is expressed by a Gaussian form (following *Kopf et al.* [2008]), which superposes onto a Chapman layer. The entire profile function is written as

$$N(z) = N_m \exp\left[\frac{1}{2}\left(1 - \frac{z - z_m}{H} - \exp\left(-\frac{z - z_m}{H}\right)\right)\right] + N_t \exp\left[-\frac{1}{2}\left(\frac{z - z_t}{H_t}\right)^2\right], \quad (1)$$

$$N_t < N_m, z_t > z_m$$

where z is altitude; N_m and z_m are the peak density and peak height of the main layer, respectively; H is the neutral atmosphere scale height; N_t and z_t are the peak density and peak height of the top layer, respectively; H_t describes the height thickness of the top layer.

The first term on the right side of Eq. (1) is an expression of the Chapman model, which is explained by several authors (e.g., *Fox and Yeager* [2006] and *Withers* [2009]). This formula is used in Eq. (1) because, for $85^\circ \leq \text{SZA} < 98^\circ$, the M2 layer is sunlit and photoionization plays a role [*Withers*, 2009; *Lillis et al.*, 2009]. Previous studies suggest that the Chapman model is applicable to the lower part of the M2 layer up to a SZA of 100° [*Němec et al.*, 2011].

In Eq. (1), the plasma density (N , m^{-3}) is related to the plasma frequency (f_p , Hz) by [*Boyd and Sanderson*, 2003]:

$$f_p^2 = 80.64N. \quad (2)$$

The measured roundtrip time delay (τ , s) at the sounding frequency (f , Hz) is related to the real height (z , m) by [*Boyd and Sanderson*, 2003]:

$$\tau(f) = \frac{2}{c} \int_0^{z_{sc}-z} \frac{dz}{n(f, z)} = \frac{2}{c} \int_0^{z_{sc}-z} \frac{dz}{\sqrt{1 - f_p^2(z)/f^2}}, \quad (3)$$

where c is the speed of light in vacuum, z_{sc} is the spacecraft altitude, and n is the refractive index of the ionospheric plasma as a dielectric medium for propagation of electromagnetic waves. The wave propagates if $f > f_p$, and it is reflected when $f = f_p$, according to the cold plasma dispersion relation [*Boyd and Sanderson*, 2003]. Therefore, the plasma frequency at the reflection point equals the wave frequency of the received echo from that point.

Equation (1) has 4 unknown parameters: z_m , H , z_t and H_t (assume N_m and N_t can be extracted from the data). Therefore, in principle, the profile can be determined with four or more measurements. The inversion retrieves the parameters by solving Eq. (3) using

measured pairs of (f, τ) . In practice, the data characteristics, combined with the non-monotonic nature of Eq. (1), render the inversion difficult in most cases. The reasons are specified in Sec. 3.2.2.

3.2.2. The Simplified Model

Equation (1) is difficult to invert in our situation because of the following two limitations.

(1) Inspections of Eqs. (1) and (3) reveal that the inverse problem is ill-conditioned.

This observation is attributed to two sources. First, the time delays of the waves that travel through the top layer can be insensitive to the shape and height of this layer. Specifically, a narrower but denser layer may produce the same time delay as that of a somewhat wider but sparser layer for a passing wave; a substantial shift of the height of the top layer may not significantly change the time delay for passing waves.

Secondly, the time delays of the waves that are reflected from the topside of the lower Chapman layer can be insensitive to the shape of the Chapman layer. For example, if z_m increases and H decreases by a certain amount simultaneously, then the height of a reflection point may remain almost unchanged.

The two “forward insensitivities” imply an ill-conditioned inverse problem. In other words, the solution (parameters to be estimated) can be sensitive to small errors in the data (small errors in the data may lead to large deviations in the solution) [Engl *et al.*, 1996]. The combination of the two sources may worsen the outcome.

(2) To reconstruct the profile, it is necessary for the measurements to cover the profile well. In particular, more than one measurement of the top layer is needed to constrain its shape and height. Such measurements correspond to the low sounding frequencies.

Unfortunately, the MARSIS ionograms are habitually more disturbed at low frequencies than at high frequencies. In our selected dataset, only 22 (~0.44%) measurements exhibit discernable echo traces from the top layers. Despite the small sample, a few are quite clear (as exemplified in Fig. 3a); but most are diffuse and incomplete (as exemplified in Fig. 3b). In more than 99.5% of the selected ionograms, echo traces from the top layer are unseen (Fig. 2).

These limitations hamper the inversion of Eq. (1), especially the reconstruction of the

top layer profile, in most cases. It is necessary to find an appropriate substitute for Eq. (1) such that the information of interest can be retrieved via an inversion, and the existing data can be used as much as possible. This goal can be achieved if the upper portion of the profile, above and within the top layer, is “temporarily” assumed to be a uniform plasma slab. The reasoning is provided as follows.

Equation (3) holds for any continuous density profile if $f > f_p$. Let $z_1 < z_t$ be a specific reflection point in the profile. From Eq. (3), we obtain (according to the integral mean value theorem):

$$\tau(f) = \frac{2(z_{SC} - z_1)}{c\sqrt{1 - f_p^2(\zeta)/f^2}}, \quad (4)$$

where ζ is an existing (but unspecified) height between z_{SC} and z_1 , and $f_p^2(\zeta)$ is therefore a fixed (albeit unknown) value. Thus, if the function $f_p^2(z)$, $z > z_1$ is replaced with an appropriate constant ($f_p^2(\zeta)$), then the same time delay can be obtained for $f > f_p$.

Therefore, we can use

$$N(z) = \begin{cases} N_{top}, & \text{if } z > z_1 \\ N_m \exp\left[\frac{1}{2}\left(1 - \frac{z - z_m}{H} - \exp\left(-\frac{z - z_m}{H}\right)\right)\right], & \text{otherwise} \end{cases} \quad (5)$$

as a substitute for Eq. (1) to perform the inversion, where $N_{top} = f_p^2(\zeta)/80.64$ is a parameter to be estimated. N_{top} is a density value between the minimum and maximum densities of the profile segment from z_1 to z_{SC} . To first order, the magnitude of N_{top} satisfies

$$N_{top} \approx \left(\langle N(z) \rangle^2 + V[N(z)]\right)^{1/2}, \quad z_{SC} > z > z_1, \quad (6)$$

where $\langle N(z) \rangle$ is the mean value of $N(z)$, and $V[N(z)]$ is the variance of $N(z)$. The proof of Eq. (6) is as follows. Using Eqs. (2), (3) and (4), we obtain

$$\frac{2(z_{SC} - z_1)}{c\sqrt{1 - 80.64N_{top}/f^2}} = \frac{2}{c} \int_0^{z_{SC} - z_1} \frac{dz}{\sqrt{1 - 80.64N(z)/f^2}}.$$

After expansion (using the expression $1/\sqrt{1-x^2} = 1 + x^2/2 + 3x^4/8 + \dots$, $0 < x < 1$), the first two terms are retained:

$$(z_{SC} - z_1) + \frac{(z_{SC} - z_1)}{2} \left(\frac{80.64 N_{top}}{f^2} \right)^2 \approx \int_0^{z_{SC} - z_1} \left[1 + \frac{1}{2} \left(\frac{80.64 N(z)}{f^2} \right)^2 \right] dz,$$

which is

$$N_{top}^2 \approx \frac{1}{z_{SC} - z_1} \int_0^{z_{SC} - z_1} [N(z)]^2 dz = \langle N^2(z) \rangle. \quad (7)$$

We can set the densities in the profile segment as a population of random values (neglecting their spatial positions) and calculate the variance:

$$V[N(z)] = \langle N^2(z) \rangle - \langle N(z) \rangle^2. \quad (8)$$

Substituting Eq. (8) into Eq. (7) produces Eq. (6). Equation (6) implies that the time delay of a wave propagating through a plasma profile is basically determined by the average density and the density variation magnitude of that profile.

Equation (5) suggests that the entire density profile can be considered to be composed of two parts separated at z_1 ($z_m < z_1 < z_i$). The upper part is a homogenous plasma slab of density N_{top} , and the lower part is a Chapman form truncated at z_1 . Equation (5) is illustrated in Fig. 4 for clarity. Equation (5) may be called a “calculation model” instead of a physical model because the uniform slab is obviously non-physical. The partition is also non-physical, which breaks the continuity of the real ionosphere. The slab is understood to be an equivalent of the real profile segment between z_1 and z_{SC} in only one way (i.e., they produce the same time delay if a wave travels through them). If Eq. (5) is used to simulate an ionogram, then the portion of the resultant echo trace that corresponds to the slab is artificial, but the portion below z_1 can be physical.

The usefulness of Eq. (5) is as follows. Equation (5) is amenable to the realistic situations in which echoes from the top layers are absent. It is free from the first source of ill-conditionedness (although the second source is still present). The profile portion below z_1 can be reconstructed correctly because the slab is equivalent to the real profile portion above z_1 regarding time delays. If z_1 is set to correspond to the second cusp (as exemplified in Fig.

2), then z_1 is lower than z_t (the peak height of the top layer) by Δz_1 , which is the height width of the density valley beneath the top layer (Fig. 4). The value of Δz_1 cannot be estimated by an inversion, but it may be estimated by other means (see Sec. 5.1.4). z_1 may serve as a boundary above which the top layers occur. The plasma density at z_1 is denoted by N_1 , which is only slightly greater than N_t (the peak density of the top layer). “Slightly” refers to an amount smaller than $(\Delta f)^2 / 80.64 \text{ m}^{-3}$, where Δf is the frequency resolution of MARSIS. N_1 is also the largest density value in the profile segment that is covered by the supposed slab. N_{top} is a “synthetic” parameter that reflects the combined effect of the average plasma density and density variation magnitude in the upper portion of the ionosphere (Eq. (6)). N_{top} is related to the spacecraft altitude z_{SC} (Eq. (10)), and the effect of z_{SC} must be removed when N_{top} is physically interpreted.

3.2.3. Inversion Algorithm

We let z_1 , the separating height between the upper slab and the lower Chapman layer, correspond to a measurement of (f_1, τ_1) . This simplifies the inversion process because only two parameters, z_m and H , remain unknown in Eq. (5). Specifically, given these two parameters, z_1 and N_{top} can be determined via Eqs. (2) and (5) with the measurement (f_1, τ_1) alone. Thus, we need only two independent measurements, which must include (f_1, τ_1) corresponding to z_1 , to determine Eq. (5), in principle. Let (f_2, τ_2) be the second measurement that corresponds to a height z_2 . Using Eqs. (3) and (4), the system to be solved is expressed as:

$$\begin{cases} F_1 = \frac{h_{SC} - z_1}{\sqrt{f_1^2 - f_{p,top}^2}} - \frac{\tau_1 c}{2f_1} = 0 \\ F_2 = \frac{h_{SC} - z_1}{\sqrt{f_2^2 - f_{p,top}^2}} + \int_{z_2}^{z_1} \frac{dz}{\sqrt{f_2^2 - f_p^2(z)}} - \frac{\tau_2 c}{2f_2} = 0 \end{cases}, (9)$$

where F_j ($j = 1, 2$) is introduced for reference only. To solve Eq. (9), we search a broad, empirically initialized parameter space for a combination of z_m and H to minimize the quantity $Q = F^2 = F_1^2 + F_2^2$. Hereafter, we call the pair (z_m, H) a solution, and call the quantity Q total fit. Q has unit of $(m \cdot s)^2$ or $(km \ ms)^2$ and quantifies the combined estimation error in time and space. The integral term in Eq. (9) can be calculated by a trapezoidal method; z_1 and z_2 are calculated via Eq. (5) by a simple iterative procedure. The search space is reduced step by step until a predefined error requirement is reached. The error requirement is simply $\Delta z_m < 0.2$ km (i.e., the reduction interval of the search for the optimal value of z_m has a final span of < 0.2 km before the search process terminates).

Equation (9) presents the second source of the ill-conditionedness (see Sec. 3.2.2), which may cause instability in the system and lead to unphysical solutions (e.g., $N_{top} < 0$). Figure 5a displays the ill-conditioned characteristics, whereby we see that in the $z_m - H$ space, a decrease in H accompanied by an increase in z_m may provide similar, apparently well-fit solutions. Due to the ill-conditionedness, a best fit solution can be unreliable.

To mitigate the ill-conditionedness, we use more than two measurements to estimate z_m and H (least squared) for each ionogram. Equation (9) is changed to:

$$\begin{cases} F_1 = \frac{h_{SC} - z_1}{\sqrt{f_1^2 - f_{p,top}^2}} - \frac{\tau_1 c}{2f_1} = 0 \\ F_j = \frac{h_{SC} - z_1}{\sqrt{f_j^2 - f_{p,top}^2}} + \int_{z_j}^{z_1} \frac{dz}{\sqrt{f_j^2 - f_p^2(z)}} - \frac{\tau_j c}{2f_j} = 0, j = 2, \dots, m \end{cases}, (10)$$

where m is the number of measurements used. In practice, $m = 5$ (five data points were extracted from each ionogram; see Sec. 2.1.3). The numerical procedure to solve Eq. (10) remains the same as that for Eq. (9). Figure 5b illustrates the solution to Eq. (10) for the same

ionogram shown in Fig. 5a. Comparing Fig. 5a and 5b reveals that more measurements reduce the ill-conditionedness, and the uniqueness of the optimal solution is clearer. Note that Eq. (10) can still be ill-conditioned. In Fig. 5b, the optimal solution lies in a nearly flat region in the solution space, which indicates a risk of instability. However, unstable cases occur rarely and do not hinder the use of Eq. (10), as will be shown later (Sec. 4.1).

An example of a simulated vertical reflection trace using the inverted parameters $H = 8.17$ km, $z_m = 160.68$ km, $z_1 = 199.02$ km and $N_{top} = 2.22e+9$ m⁻³ based on Eq. (10) is included in Fig. 2. For this inversion, the total fit Q is $5.0649e-6$ (km ms)², which can be interpreted as an error of approximately $2.25e-3$ km times microsecond. The error is small, and the simulated trace conforms well to the observed trace; thus, the retrieved parameters can be regarded as feasible. However, in the low frequency portion, where the ionospheric echo trace is invisible, the simulated trace corresponds to the assumed slab and is artificial.

For more than 89% of the 4988 frames, Q is smaller than $2.45e-4$ (km ms)² (Fig. 6a). We can further evaluate the effectiveness of the inversions using the composite correlation coefficient (R), which is calculated as $R = [(D - Q) / D]^{1/2}$ where $D = \sum_{j=1}^5 (F_j - \langle F \rangle)^2$ and $\langle F \rangle = (\sum_{j=1}^5 F_j) / 5$. The value of R ranges between 0 and 1. A greater value of R indicates a better fit. For more than 95% of the frames, $R > 0.955$ (Fig. 6b); therefore, the inversions are highly effective.

4. Results

Using the data extraction and inversion method described in Sec. 2 and Sec. 3, we obtained values for the ionospheric parameters of N_m , z_m , H , z_1 , N_1 and N_{top} for each frame. This results in a new, large dataset that enables a statistical examination of variations and mutual relationships of the parameters.

4.1. Variations of N_m , z_m and H with SZA and the Martian Seasons

The parameters N_m , z_m and H describe the main body of the M2 layer and have been the central objectives of previous studies of the M2 layer [e.g., Gurnett, et al, 2005; Zou et al., 2005; Fox and Yeager, 2006; Morgan et al., 2008; Němec et al., 2011]. Therefore, the seasonal and SZA variation trends of these parameters in the daytime ionosphere, including the near-terminator region, are considered well known. We shall compare our results with the previous results to determine the consistency and variation in the near-terminator region in the presence of a top layer.

4.1.1. SZA Variations

The variations of N_m , z_m and H with SZA are shown in Fig. 7. In this density plot, the data point numbers in equal-spaced, small coordinate intervals (e.g., 0.1° SZA \times $0.06 \times 10^3 N_m$ interval) are color-coded such that the distribution of the scatter points can be clearly observed, even if they overlap. The mean values and standard deviations of the parameters (the vertical coordinates) are calculated in contiguous equal-spaced bins of the variable (the horizontal coordinate) and displayed with a solid curve (for the mean value) or 2 dashed curves (for the mean \pm standard deviation). These conventions are followed in the subsequent density plots and scatter plots where applicable.

For clarity, the average values and standard deviations of the parameters at SZA = 85° and 95° in Fig. 7 are listed in Table 1. In Table 1, the available previous results are also listed for comparison.

Based on Fig. 7 and Table 1, we observe that within the SZA interval of 85° – 95° , N_m decreases (Fig. 7a), z_m increases (Fig. 7b), and H slightly decreases (Fig. 7c) with increasing SZA. Our results are in agreement with previous studies (Table 1).

Němec et al. [2011] suggest that the lower portion (within approximately $5H$ above z_m) of the M2 layer can be characterized as a Chapman layer (up to 100° of SZA). Our results seem to confirm the plausibility of this notion in the cases where the top layers are detected near the terminator.

4.1.2. Seasonal variations

The solar longitude (L_S) determines the seasons on Mars: $L_S = 0^\circ, 90^\circ, 180^\circ$ and 270° correspond to the northern spring equinox, summer solstice, autumn equinox and winter solstice, respectively. Figure 8 shows the variations of N_m , z_m , and H with L_S . The data coverage is patchy for L_S . Therefore, the continuous variation of the parameters with L_S is not clear. However, by comparing the average values of the parameters in the L_S regions that are data dense, coarse variation trends may be recognized. For clarity, the average values and standard deviations of N_m , z_m , and H at certain L_S ranges are summarized in Table 2. N_m , z_m and H are all greater in the northern winter than in the northern summer; z_m and H are greater in the southern spring and summer than in the southern autumn and winter, but N_m does not seem to have a significant difference in these two seasons. Previous studies of the seasonal variations of the Martian ionosphere were focused on the sub-solar region. *Morgan et al.* [2008] show that the sub-solar peak height is approximately 10 km higher, and the sub-solar peak density is approximately $4e+10 \text{ m}^{-3}$ larger in the northern winter than in the northern summer on average. *Zou et al.* [2005] found that at $L_S = 136^\circ - 146^\circ$, the sub-solar peak height is ~ 10 km lower in the northern hemisphere than in the southern hemisphere on average. These findings have similar variation trends to those in Table 2.

4.2. Variations of z_1 , N_1 and N_{top}

4.2.1. Relationship between N_1 and N_{top}

In the SZA interval of $85^\circ - 98^\circ$, the average values (standard deviations) of N_1 and N_{top} are $0.686e+10 \text{ m}^{-3}$ ($0.232e+10 \text{ m}^{-3}$) and $0.205e+10 \text{ m}^{-3}$ ($0.135e+10 \text{ m}^{-3}$), respectively. Figure 9 displays the relationship between N_1 and N_{top} , which are positively correlated. As stated in Sec. 3.2.2, N_{top} is affected by the spacecraft altitude z_{SC} . A larger z_{SC} value means that the supposed slab covers a larger portion of the low density profile; thus, N_{top} is smaller.

Additionally, the relationship between N_1 and N_{top} can be obscured by averaging. In Fig. 9, the scattered data points spread as z_{SC} increases and manifest the expected trend that N_{top} decreases with increasing z_{SC} . Obviously, if the effect of z_{SC} was removed (e.g., by restricting z_{SC} to a small interval), then the positive relationship between N_1 and N_{top} could be clearer. Therefore, we assume that N_{top} is basically determined by N_1 , although it represents the sum of all dispersion elements between z_1 and z_{SC} (Sec. 3.2.2). In the following sections, N_{top} is ignored.

4.2.2. SZA variations

In the SZA interval of 85° - 98° , the overall average values (standard deviations) of z_1 and N_1 are 187.98 km (18.32 km) and $0.68\text{e}+10 \text{ m}^{-3}$ ($0.27\text{e}+10 \text{ m}^{-3}$), respectively. Because the overall average value of z_m is approximately 141 km (Sec. 4.1.1), we assume that the first top layer tends to occur at altitudes that are $\sim 47 + \Delta z_1$ km above the main peak (Δz_1 is indicated in Fig. 4 and will be estimated later (Sec. 5.1.4)).

Figure 10 displays N_1 (a) and z_1 (b) sorted by SZA. In this figure, a distinct dependence of N_1 and z_1 on SZA does not appear.

4.2.3. Seasonal variations

Figure 11 plots N_1 (a) and z_1 (b) against L_s . The data coverage for L_s is patchy, similar to Fig. 8. We again inspect the L_s regions where the data are dense to find coarse trends, which are summarized in Table 3. N_1 is greater in the northern winter than in the northern summer; z_1 is higher in the southern spring than in the southern autumn (Table 3). A comparison of Figs. 11 and 8 indicates that N_1 and z_1 have seasonal variation trends that are similar to those of N_m and z_m , respectively.

4.2.4. Relationships between the Parameters

In this subsection, we investigate the relationships of N_1 and z_1 with N_m , z_m and H to examine how the top layer is related to the underlying main layer.

Figure 12 illustrates the relationship between N_1 and N_m . Although obscured by large deviations of N_1 , it appears that N_1 increases with N_m . This trend implies that the height difference $(z_1 - z_m)$ tends to be constant or nearly constant, because otherwise N_1 cannot be predicted by the monotone-decreasing Chapman formula between z_1 and z_m (Eq. (5)).

Figure 13 presents a scatter plot of the relationship between z_1 and z_m , wherein the value of H that corresponds to each data point is color-coded. In this figure, a positive relationship exists between z_1 and z_m . Additionally, z_1 increases with increasing H . If H was limited to a small interval, then the trend that z_1 increases with increasing z_m would be more prominent. This trend again implies that the height difference $(z_1 - z_m)$ tends to be nearly constant.

Figure 14 presents the occurrence frequency distribution of the (a) values of $(z_1 - z_m)$ and (b) values normalized by H . The values of $(z_1 - z_m)$ are quite concentrated around their mean value of ~ 47 km (with a standard deviation of ~ 18 km) (Fig. 14a). The mean value of $(z_1 - z_m)/H$ is 4.28 (with a standard deviation 0.72) (Fig. 14b), which is roughly comparable to the bottom altitude boundary ($\sim 5H$) of the “transitional region” of the daytime M2 layer that was suggested by *Němec et al.* [2011]. A comparison of Figs. 14a and 14b indicates that the occurrence distribution of $(z_1 - z_m)/H$ appears more concentrated than that of $(z_1 - z_m)$. This is consistent with the observation that $(z_1 - z_m)$ and H are positively associated, as shown in Fig. 13. This positive relationship is more clearly shown in Fig. 15: as H increases from ~ 5 km to ~ 20 km, $(z_1 - z_m)$ increases from ~ 20 km to ~ 80 km. Figures 13, 14 and 15 suggest that fluctuations in H are likely a main factor that affects the variations of the height of

the top layer.

5. Discussion

In this subsection, we attempt to explain the findings demonstrated above (Sec. 4) and discuss the associated uncertainties. The explanations are qualitative and tentative due to the complexity of the issues concerned.

5.1. Explanations

5.1.1. Explanation of the Seasonal and SZA Variations of N_m , z_m and H

The dependence of N_m , z_m and H on SZA, as shown in Fig. 7, was identified and explained in several studies using photoionization-electron impact ionization models [e.g., *Fox and Yeager*, 2006; *Morgan et al.*, 2008]. We believe that the existing explanations are applicable to our results (Fig. 7). The main points are as follows. As the SZA increases, the solar radiation-induced photoionization (and electron impact ionization) production rate decreases; therefore, N_m decreases (Fig. 7a). The density peak occurs where the production rate is maximal. This position rises with increasing SZA, so z_m increases with SZA (Fig. 7b). The neutral scale height H is proportional to the neutral temperature. As SZA increases, the solar radiation is reduced and the atmosphere cools down; hence, H decreases (Fig. 7c).

The phenomenon that N_m , z_m and H are greater in the northern winter than in the northern summer (Fig. 8) may be explained by the thermal atmosphere model of Mars as described by *Bougher et al.* [2006]. Above 100 km altitude in either hemisphere of Mars, the air temperature is several tens of Kelvin higher during the north winter solstice than during the north summer solstice. Therefore, in the winter, H is larger (Fig. 8c). In turn, the isobars are elevated in the atmosphere and z_m increases (Fig. 8b). A higher atmospheric temperature is positively related to ionization, but negatively related to recombination [*Rishbeth and Garriott*, 1969]; thus, N_m increases (Fig. 8a).

The phenomenon that z_m is higher in the southern spring than in southern autumn (see

Fig. 8b) was previously identified and explained by several authors [e.g., *McElroy et al.*, 1977; *Wang and Nielsen*, 2003b, and references therein]. We believe those explanations are also applicable to our results (Fig. 8). In the southern spring and summer, dust storms prevail [*Kahn et al.*, 1992; *Smith*, 2004]. Dust suspended in the lower atmosphere promotes solar heating and expansion of the lower atmosphere. This may enhance the neutral density in the upper atmosphere, which provides more materials (O, O₂ and CO₂) for photoionization at high altitudes, but reduces solar radiation at lower altitudes. Therefore, z_m is elevated (Fig. 8b), but N_m may remain unchanged [*Wang and Nielsen*, 2003b] (Fig. 8a). During this process, the neutral pressure scale height H may also increase in the upper atmosphere (Fig. 8c), even if the neutral temperature was not raised, because H is equal to the neutral density scale height in an isothermal atmosphere.

Based on the above phenomena, it appears that the SZA and seasonal variations of the main body of the M2 layer remain “normal” as the SZA increases up to 98°, irrespective of the presence of a top layer.

5.1.2. Explanation of the variations of N_1 and z_1

The variations of z_1 and N_1 may provide clues of the origin of the top layer. Regarding the origin of the top layers, the existing explanations mainly resort to external forces, such as interactions of the solar wind with the main layer ionosphere, as mentioned in introduction. As revealed in Sec. 4, however, N_1 and z_1 are correlated to N_m , z_m and H ; that is, the variations of the top layer are associated with variations of the main layer. This indicates that some “internal” processes may also be important for the formation of the topside layer(s). It is well known that the ionosphere is in quasi-equilibrium between ionization and recombination near the main density peak, whereas plasma transport dominates ~100 km above the main peak. Thus, somewhere in the transitional region, the two mechanisms may be comparably prevalent [e.g., *Gurnett et al.*, 2008; *Morgan et al.*, 2008; *Withers*, 2009; *Němec et al.*, 2011]. In this two-process region, the section of the plasma that is produced by photoionization and electron impact ionization may be assumed stationary (i.e., zero average velocity), while the

transported section drifting upward. Thus, a local beam-plasma system might form, whereby a beam-plasma instability may develop. The instability, if incurred, would be a growing (with time) electrostatic wave. Because ions move much slower than electrons, we assume the ions are a static neutralizing background, and the transported electrons are the beam that flows through the stationary electrons. According to the cold plasma wave theory, instability occurs for

$$k < k_c = [1 + (\omega_{pb} / \omega_p)^{2/3}]^{3/2} \omega_p / v_b, \quad (11)$$

where k is the wave number of the perturbed wave, k_c is the critical wave number, ω_p is the (angular) plasma frequency of the stationary section, ω_{pb} is the (angular) plasma frequency of the beam, and v_b is the drift velocity of the beam [Boyd and Sanderson, 2003]. Around a 200 km altitude, the plasma frequency of the stationary section (f_p) is typically about 0.5e+6 MHz. Thus, $\omega_p (= 2\pi f_p)$ is about $3e+6 \text{ s}^{-1}$. Supposing that the beam drift speed v_b is near 200 km s^{-1} and ω_{pb} is comparable to or smaller than ω_p , then k_c is $\sim 40 \text{ m}^{-1}$. For a growing wave of wavelength $\lambda \sim 10 \text{ km}$ (a value comparable to the width of the top layer, as estimated by Kopf *et al.* [2008] with a daytime ionogram in which the echo traces from the topside of the top layer are clear), $k = 2\pi / \lambda \approx 0.0006 \text{ m}^{-1} < k_c$.

It appears that instability can always occur as Eq. (11) can be easily satisfied by long wavelength waves and by small beam velocities. This is due to the cold plasma approximation which neglects thermal effects. Factually, according to the kinetic theory, v_b should be greater than the thermal speed of the electrons (v_{th}) for instability to occur; otherwise, the beam may be diffused by the thermal motion of the electrons [Boyd and Sanderson, 2003]. At a 200 km altitude, the electron temperature (T_e) is about 1000 K [Withers, 2009]; thus, the electron thermal speed is $v_{th} = \sqrt{k_B T_e / m_e} \approx 120 \text{ km s}^{-1}$, where $k_B = 1.381e-23 \text{ J K}^{-1}$ is Boltzmann's constant and $m_e = 9.109e-31 \text{ kg}$ is the electron mass.

In short, it might be possible for a beam-plasma instability to occur if there are a certain

amount of electrons collectively drifting upward with a velocity of a few hundred km s⁻¹. The instability may form a local ascension in the electron density, which could appear as a layer.

The above hypothesis, together with the photo- and electron impact ionization mechanisms [e.g., *Fox and Yeager, 2006*] and the plasma diffusion theory [*Rishbeth and Garriott, 1969*], seems to explain most of the phenomena demonstrated in Sec. 4. During the development of the instability, the electron density in the perturbed wave may continue growing until the electric field created by “electron bunching” becomes large enough to scatter the electrons and to disperse the drift velocity of the beam when the instability is extinguished [*Boyd and Sanderson, 2003*]. Moreover, the transport of the beam electrons is related to ambipolar diffusion (i.e., the electron cloud cannot travel upward constantly because it is restrained by the slow-moving ions) [*Rishbeth and Garriott, 1969*]. Therefore, the top layer should be transient (as discovered by *Kopf et al. [2008]*). If above the first top layer, ionization still plays a significant role, a similar process may occur such that more than one top layer forms. The maximum growth rate (γ_{\max}) of the instability is positively related to α_p and α_{pb} ($\gamma_{\max} \approx \sqrt{3}(\omega_p \omega_{pb}^2)^{1/3} / 2^{4/3}$ [*Boyd and Sanderson, 2003*]). At high altitudes (e.g., >230 km), α_p is small; thus, γ_{\max} is small. However, at low altitudes (e.g., < 170 km), v_b is zero. Therefore, the top layer may tend to occur at a certain distance ($z_1 - z_m$) from the main peak (here, we ignore Δz_1 , which is discussed in Sec. 5.1.4). A larger neutral scale height H implies a weaker diffusion (the diffusion coefficient is $D(z) \propto \exp[(z - z_{\text{ref}})/H]$, where z_{ref} is an arbitrary reference height [*Rishbeth and Garriott, 1969*]). In other words, if H is large, then a large distance ($z_1 - z_m$) is required to guarantee the outset of transport; whereas the beam is related to the transport. Therefore, the distance ($z_1 - z_m$) is positively related to H (Fig. 15), and the occurrence frequency distribution of $(z_1 - z_m)/H$ is concentrated (Fig. 14). Because the height difference ($z_1 - z_m$) is concentrated around a constant, N_1 and z_1 are roughly predictable by N_m and z_m , respectively (Figs. 12 and 13), according to the Chapman formula (Sec. 4.2.4).

As the SZA increases from 85° to 98° , at high altitudes above the main peak near z_1 (approximately 190 km), the solar flux for photoionization may not change much because the optical length is small [Rishbeth and Garriott, 1969]. However, at lower altitudes near z_m (approximately 140 km), the solar flux changes significantly within the SZA interval. At these lower altitudes, N_m and z_m change with the increasing SZA in such a way that the lower side of the Chapman-shaped profile shrinks upward, but its upper side moves much less (see [Fox and Yeager, 2006]). Thus, N_1 and z_1 appear to be independent of the SZA (Fig. 10). This independence means that, with the changing SZA, the positive relationship between N_1 and N_m (Fig. 12) and between z_1 and z_m (Fig. 13) does not behave. However, these relationships would behave with the changing seasons as N_1 and z_1 have seasonal trends similar to those of N_m and z_m , respectively (Figs. 8 and 11). In the northern winter and southern spring, the neutral atmosphere was heated and/or elevated more or less bodily (Sec. 5.1.1), and the M2 layer could also be elevated bodily. Thus, when N_m , z_m and H increased (Fig. 8), z_1 and N_1 also increased (Fig. 11); the height difference ($z_1 - z_m$) was mostly maintained. Hence, we see the positive relationship between N_1 and N_m (Fig. 12) and between z_1 and z_m (Fig. 13).

It is possible that external factors, such as neutral winds, gravity waves and/or solar wind pressure fluctuations [Wang and Nielsen, 2003a], may trigger the occurrence of the instability. For example, when H is suddenly reduced, some strong diffusion transport may be initiated somewhere on the topside of the M2 layer, and a collective motion of electrons may possibly occur at the initial stage of the ambipolar diffusion. It is also possible that abnormal solar wind streams result in the top layers by two-stream instabilities that may develop in the transportation region. However, the regularities demonstrated in Sec. 4.2 seem to be unfavorable for explanations by external factors alone.

Kopf *et al.* [2008] report that the occurrence rate of the top layer(s) in the daytime is decreasing toward the terminator. In the present work, only a SZA interval of 85° - 98° is involved, and we did not correlate the occurrence rate to the SZA. The reason is that if a

second cusp is not observed in an ionogram, we generally cannot conclude the absence of a top layer; the absence of the cusp may be due to disturbances and/or the detection limit of MARSIS (see Sec. 2.2), as well as the absence of a top layer. Nevertheless, the apparently low occurrence rate of the top layers is unexplained. A possible explanation is that the occurrence of a beam-plasma instability requires a collective motion of electrons at a high velocity (e.g., $>200 \text{ km s}^{-1}$), and such a requirement is not easily fulfilled, which limits the occurrence rate of the top layers in general.

5.1.3. Influence of the Crustal Magnetic Field on N_m and N_1

We determined if the weak crustal magnetic fields of Mars influence the plasma layers in our data. Among the ~ 5000 selected frames, 1057 ($\sim 21\%$) exhibit more than one electron cyclotron echo (see Fig. 2 for an example). For each of these frames, the electron cyclotron frequency (f_c , in Hz) at the spacecraft position can be obtained by measuring the electron cyclotron echo period [Gurnett *et al.*, 2005]. f_c varies within 300 – 1200 Hz in most cases ($>99\%$), which corresponds to an in situ magnetic field strength (B) range of approximately 10 – 40 nT ($f_c = 28B$ [Gurnett *et al.*, 2005]). Figure 16 displays N_m (a) and N_1 (b) against f_c , where the spacecraft altitude (z_{SC}) that corresponds to each data point is color-coded. In this figure, no significant dependence of N_m and N_1 on f_c is apparent for the entire spacecraft altitude range (approximately 300 – 1000 km) nor for small intervals of z_{SC} . This result agrees with Kopf *et al.* [2008] who report that no clear relationships were found between the top layers and the crustal magnetic field.

5.1.4. Possible Magnitude of Δz_1

The height of the top layer has not been determined because the quantity Δz_1 (as indicated in Fig. 4) is difficult to invert. However, because the profile is generally assumed to be monotone-increasing upward from the main peak [e.g., Gurnett *et al.*, 2008; Morgan *et al.*,

2008; Withers, 2009; Němec *et al.*, 2011], Δz_1 may be considered small. Furthermore, many of the MGS RS density profiles [Tyler *et al.*, 2001] exhibit significant density peaks on the topside of the M2 layer. There are 55,014 profiles in total, and they can be downloaded at <http://pds-geosciences.wustl.edu/missions/mgs/radioscience.html>. Of all of the profiles, 282 have a SZA $\geq 85^\circ$, among which ~ 120 (42.6%) exhibit notable topside peaks. The peaks occur mainly at altitudes of 160 – 220 km (usually with a ~ 10 km thickness). We propose that the peaks are most likely the same as the transient layers observed by MARSIS. The occurrence rate of them in the MGS data is much higher than that (1.86%) in the MARSIS data, because the MARSIS ionograms are often obscured by noise in the lower frequency portions thus the top layer echoes are indiscernible, as stated in Sec. 2.2. Figure 17 illustrates three examples of MGS RS profiles in which the magnitude of Δz_1 (equivalent to that indicated in Fig. 4) is on the order of 10 km. Because the average value of z_1 is ~ 190 km (Sec. 4.2.2), we assume that the height position of the first top layer tends to be near $z_1 + \Delta z_1 = 200$ km.

5.2. Uncertainties

Uncertainties in the individual data points and in the trends of Figs. 7 through 15 may arise from various sources:

(1) Errors in the data are mainly those inherent in the MARSIS AIS measurements. The accuracy of the measurements of plasma density is approximately $\pm 2\%$ because the sounding frequencies are spaced at $\Delta f / f \approx 2\%$ [Němec *et al.* 2011]. Therefore, the relative errors in the plasma densities (N_m, N_1) are $\sim 4\%$ (due to Eq. (2)).

The receiving time bins are $\Delta \tau = 91.3 \mu\text{s}$; therefore, the possible errors in the time delays are approximately $\pm 45 \mu\text{s}$. The errors in the time delay may cause different errors in the distance, depending on the value of the ratio f_p^2 / f^2 . For $f_p^2 / f^2 = 0.1$ and 0.9 , a $45 \mu\text{s}$ error in the time delay produces a distance error of approximately 6.4 km and 1.5 km, respectively (using Eq. 4). Therefore, the absolute distance error due to the possible time delay error is approximately ± 4 km on average, and the relative error is typically $\sim 3.6\%$ for

z_m and $\sim 2.6\%$ for z_1 (z_m and z_1 are typically approximately 140 km and 190 km, respectively).

The actual relative errors in z_m and z_1 are larger by approximately 2% due to the addition of errors in the refractive index $\sqrt{1-80.64N/f^2}$ (Eq. (4)) (2% for typical values of $80.64N/f^2=0.5$). Thus, we can say that z_m and z_1 may have relative errors within approximately 6% (or absolute errors within ~ 11 km). In Figs. 10 and 11, we note that the standard deviations of z_m and z_1 at a 1° SZA or 30° L_S bin are approximately 15 km. Therefore, the errors in the data may be a major contributor to the large spread of the parameters. We can assume that the probability distributions of the data errors are Gaussian-like (positive and negative errors are comparably probable). Thus, the errors may not greatly affect the average values (the variation trends) concerned.

(2) Due to the ill-conditionedness of the inverse problem, small errors in the data may be magnified in the estimates of z_m , z_1 and H (N_m and N_1 are not affected because they were extracted instead of inverted). This magnification is difficult to quantify, but the ~ 100 ($\sim 2\%$) extreme values of H (3.2 km and 23.5 km) in Figs. 7c, 8c and 15 represent the maximum magnification that corresponds to the acceptable error threshold of <0.2 km of z_m during optimization (Sec. 3.2.3). These extreme values indicate that the system (Eq. 10) was unstable while obtaining these values. All of the other best fit solutions potentially included errors. Therefore, the ill-conditionedness of the inverse problem may contribute to the spread of the z_m , z_1 and H values, although the least square approach mitigates this effect. However, this shortcoming's influence on the variation trends of z_m and z_1 can be expected to be negligible because the errors it causes are also Gaussian-like (as indicated by the fact that the extreme values of H occur at both ends – small and large).

(3) The variation trends in Figs. 7 – 15 can be examined by t -tests. The suggestion that “ N_1 is larger in the northern winter than in the northern summer” exhibited in Fig. 11b and Table 3, for instance, is tested as follows. Using the data displayed in the first two rows of Table 3, the t -test statistic is calculated as 14.52, which is much greater than the threshold of $<$

2.68 at the confidence level of 0.005. The conclusion of this test is that the two mean values are significantly different at a high confidence level. Thus, the proposed trend is significant at a high confidence level. All of the relationships suggested in Sec. 4 were statistically significant at high confidence levels (0.005) when tested in this manner.

The trends reveal statistical relationships. They can be used to predict the average values of a large number of samples, but they are not capable of predicting any individual data point precisely because of the large deviations accompanying them.

(4) The large spread of data may also be associated with the effects of the various other factors (Mars topography, longitude, etc.) as mentioned in the introduction, which are not involved in this work. We believe that the neglect of the other factors does not present an obstacle to finding the variation trends in Sec. 4; when the data are sorted by a factor to examine the variation of a parameter via the statistical pattern, the influences of the other factors may be mostly canceled out by averaging.

6. Conclusions

The peak density (N_m), peak height (z_m) and the neutral scale height (H) of the main body of the M2 layer can be effectively estimated by an inversion method that assumes the unseen (by MARSIS), non-monotonic upper portion of the density profile is a homogenous slab. An analysis of ~5000 selected MARSIS ionograms indicates that the main body of the M2 layer, located ~10 km below the first topside transient layer and above the main peak, may be well characterized as a Chapman layer near the terminator ($SZA = 85^\circ - 98^\circ$), notwithstanding a high SZA condition and the presence of the top layer. The first top layer above the main peak tends to occur ~60 km (with a standard deviation of ~20 km) above the main peak. The peak density (N_1) and peak height (z_1) of the first top layer are positively related to N_m and z_m , respectively. N_1 and z_1 appear to be independent of the SZA, but they possess seasonal variation trends similar to those of N_m and z_m , respectively. z_1 is higher (by ~10 km) in the southern spring and summer than in the southern autumn and winter, indicating that the height of the top layer is controlled by the underlying atmosphere, which expands in the southern

spring and summer due to dust-heating [e.g. Smith, 2004]. The statistical relationship between the parameters suggests that the formation of the topside layers may be closely related to the processes of photoionization and diffusion that occur on the topside of the M2 layer. It is possible that development of beam-plasma instabilities in the transitional region (between the lower Chapman region and the upper transport-dominating region) is a mechanism that is responsible for the occurrences of the top layers.

Notation

- c speed of light in vacuum ($=2.998e+8$ m s⁻¹)
- f wave frequency (Hz)
- f_c electron cyclotron frequency (Hz)
- f_j wave frequency in the j th extracted data point (Hz)
- f_p plasma frequency (Hz)
- $f_{p,1}$ plasma frequency at the height z_1 (Hz)
- $f_{p,m}$ peak plasma frequency of the main ionospheric layer (Hz)
- k wave number (m⁻¹)
- k_c critical wave number above which a beam-plasma instability may occur (m⁻¹)
- k_B the Boltzmann's constant ($=1.381e-23$ J K⁻¹)
- L_S solar longitude (°)
- m data point number
- m_e electron mass ($=9.109e-31$ kg)
- n refractive index (dimensionless)
- v_b drift velocity of an electron beam or stream (km s⁻¹)
- v_{th} electron thermal velocity (km s⁻¹)
- z height (m, km)

- z_1 height corresponding to the data point (f_1, τ_1) (m, km)
- z_b height of the bottom of the supposed uniform plasma slab (m, km)
- z_m height of the density peak of the main ionospheric layer (m, km)
- z_{SC} spacecraft height (m, km)
- z_t height of the density peak of the first topside layer (m, km)
- B magnetic field strength (nT)
- D deviation quadratic sum of F_j ((km·ms)²)
- $D(z)$ diffusion coefficient as a function of height z (m² s⁻¹)
- F_j difference between the estimated and observed quantity of $c\tau_j/2f_j$ (km·ms)
- H the neutral scale height (km)
- H_t height thickness of the first topside layer (km)
- N plasma density (m⁻³)
- N_1 plasma density at the height z_1 (m⁻³)
- N_m peak plasma density of the main ionospheric layer (m⁻³)
- N_t peak plasma density of the first topside layer (m⁻³)
- N_{top} density of the supposed uniform plasma slab (m⁻³)
- Q total fit (a quantity which controls the optimization of inversion) (km·ms)²
- R composite correlation coefficient (dimensionless)
- T_e electron temperature (K)
- $V(x)$ variance of x
- Δf frequency step of the transmitted waves of MARSIS (Hz)
- Δz_1 height difference ($= z_t - z_1$) (km)
- Δz_m acceptable error of z_m during optimization (<0.2 km)
- γ_{max} the maximum growth rate of a beam-plasma instability (rad s⁻¹)

λ wavelength (m)

α_p angular plasma frequency (rad s⁻¹)

α_{pb} angular electron oscillation frequency of an electron beam or stream (rad s⁻¹)

τ roundtrip time delay (s, μ s)

τ_j roundtrip time delay in the j th extracted data point (s, μ s)

ζ a height between z_1 and z_m at which the plasma density equals N_{top} (km)

(f_j, τ_j) the j th extracted data point, $j = 1, 2, \dots, m$

$\langle x \rangle$ mean value of x

Acknowledgements

MARSIS was built and jointly managed by the Italian Space Agency and NASA. Mars Express was built and is operated by the European Space Agency. This study is supported by the Natural Science Foundation of China (NSFC) (Project No. 41274181, No. 40874092). The authors thank the three reviewers for their constructive and insightful comments on this manuscript.

References

- Akalin, F., D.D. Morgan, D.A. Gurnett, et al., 2010. Dayside induced magnetic field in the ionosphere of Mars. *Icarus* 206, 104–111. doi:10.1016/j.icarus.2009.03.021.
- Bougher, S. W., J. M. Bell, J. R. Murphy, et al., 2006. Polar warming in the Mars thermosphere: Seasonal variations owing to changing insolation and dust distributions. *Geophys. Res. Lett.* 3, L02203, doi:10.1029/2005GL024059.
- Bougher, S. W., S. Engel, D. P. Hinson, and J. R. Murphy, 2004. MGS Radio Science electron density profiles: Interannual variability and implications for the martian neutral atmosphere. *J. Geophys. Res.* 109, E03010, doi:10.1029/2003JE002154.
- Boyd, T. J. M., Sanderson, J. J., 2003. *The Physics of Plasmas*. Cambridge University Press, 40 West 20th Street, New York, NY10011-4211, USA.

- Breus, T. K., A. M. Krymskii, D. H. Crider, et al., 2004. Effect of the solar radiation in the topside atmosphere/ ionosphere of Mars: Mars Global Surveyor observations. *J. Geophys. Res.* 109, A09310, doi:10.1029/ 2004JA0 10431.
- Dubinin, E., G. Chanteur, M. Fraenz, et al., 2008. Asymmetry of plasma fluxes at Mars. ASPERA-3 observations and hybrid simulations. *Planet. Space Sci.* 56, 832–835. doi:10.1016/j.pss.2007.12.006.
- Dungey, J. W., 1956. The effect of ambipolar diffusion in the night-time F layer. *J. Atm. Terr. Phys.* 9, 90-102.
- Duru, F., Gurnett, D.A., Averkamp, et. al., 2006. Magnetically controlled structures in the ionosphere of Mars. *J. Geophys. Res.* 111, A12204, doi:10.1029/2006JA011975.
- Duru, F., Gurnett, D.A., Morgan, et al., 2008. Electron densities in the upper ionosphere of Mars from the electron plasma oscillations. *J. Geophys. Res.* 113, A07302, doi:10.1029/2008JA013073.
- Duru, F., D.A. Gurnett, J.D. Winningham, R., et al., 2010. A plasma flow velocity boundary at Mars from the disappearance of electron plasma oscillations. *Icarus* 206, 74–82. doi:10.1016/j.icarus.2009.04.012.
- Engl, H., W. M. Hanke, A. Neubauer, 1996. *Regularization of Inverse Problems*, Kluwer Acad., Dordrecht, Netherlands.
- Fillingham, M. O., L.M. Peticolas, R.J. Lillis, 2010. Localized ionization patches in the nighttime ionosphere of Mars and their electrodynamic consequences. *Icarus* 206, 112–119. doi:10.1016/j.icarus.2009.03.005.
- Fox, J. L. and J. F. Bzannon, 1993. Upper limits to the nightside ionosphere of Mars. *J. Geophys. Res.* 20(13), 1341-1394.
- Fox, J. L., and K. E. Yeager, 2006. Morphology of the near-terminator Martian ionosphere: A comparison of models and data. *J. Geophys. Res.* 111, A10309, doi:10.1029/ 2006JA01 1697.
- Fox, J. L., K. E. Yeager, 2009. MGS electron density profiles: Analysis of the peak magnitudes. *Icarus* 200, 468–479. doi:10.1016/j.icarus.2008.12.002.
- Fränz, M., E. Dubinin, E. Nielsen, et al., 2010. Transterminator ion flow in the Martian ionosphere. *Planet. Space Sci.* 58, 1442–1454. doi: doi:10.1016/ j.pss.2010. 06.009

- Gurnett, D.A., Kirchner, D.L., Huff, R.L., et al., 2005. Radar soundings of the ionosphere of Mars. *Science* 310, 1929–1933.
- Gurnett, D. A., R. L. Huff, D. D. Morgan, et al., 2008. An overview of radar soundings of the Martian ionosphere from the Mars Express spacecraft. *Adv. Space Res.* 41, 1335–1346. doi:10.1016/j.asr.2007.01.062.
- Hanson, W.B., Sanatani, S., Zuccaro, D.R., 1977. The Martian ionosphere as observed by the Viking retarding potential analyzers. *J. Geophys. Res.* 82, 4351–4363.
- Hantsch, M.H. and Bauer, S.J., 1990. Solar control of the Mars ionosphere. *Planet. Space Sci.* 38, 539–542.
- Jordan, R., G. Picardi, J. Plaut, et al., 2009. The Mars express MARSIS sounder instrument. *Planet. Space Sci.* 57, 1975–1986. doi:10.1016/j.pss.2009.09.016.
- Kahn, R. A., T. Z. Martin, R. W. Zurek, and S. W. Li, 1992. The Martian dust cycle, *in* Mars, edited by H. H. Kieffer et al. (1992), pp. 1017–1053, Univ. of Ariz. Press, Tucson.
- Kopf, A. J., D. A. Gurnett, D. D. Morgan, et al., 2008. Transient layers in the topside ionosphere of Mars. *Geophys. Res. Lett.* 35, L17102, doi:10.1029/2008GL034948
- Krymskii, A. M., T. K. Breus, N. F. Ness, et al., 2003. Effect of crustal magnetic fields on the near terminator ionosphere at Mars: Comparison of in situ magnetic field measurements with the data of radio science experiments on board Mars Global Surveyor. *J. Geophys. Res.* 108(A12), 1431. doi:10.1029/2002JA009662.
- Lillis, R. J., H. V. Frey, M. Manga, et al., 2008. An improved crustal magnetic field map of Mars from electron reflectometry: Highland volcano magmatic history and the end of the martian dynamo. *Icarus* 194, 575–596. doi:10.1016/j.icarus.2007.09.032.
- Lillis, R. J., M. O. Fillingim, L. M. Peticolas, et al., 2009. Nightside ionosphere of Mars: Modeling the effects of crustal magnetic fields and electron pitch angle distributions on electron impact ionization. *J. Geophys. Res.* 114, E11009, doi:10.1029/2009JE003379.
- McElroy, M.B., Kong, T.Y., Yung, Y.L., 1977. Photochemistry and evolution of Mars' atmosphere: a Viking perspective. *J. Geophys. Res.* 82, 4379–4388.
- Morgan, D. D., D. A. Gurnett, D. L. Kirchner, et al., 2008. Variation of the Martian ionospheric electron density from Mars Express radar soundings. *J. Geophys. Res.* 113,

- A09303, doi:10.1029/2008JA013313.
- Morgan, D. D., O. Witasse, E. Nielsen, et al., 2013. The processing of electron density profiles from the Mars Express MARSIS topside sounder. *Radio Sci.* 48, 1-11. doi:10.1002/rds.20023.
- Nielsen, E., Wang, X.D., Gurnett, D.A., et al., 2007a. Vertical sheets of dense plasma in the topside Martian ionosphere. *J. Geophys. Res.* 112, E02003. doi:10.1029/2006JE002723.
- Nielsen, E., Fraenz, M. Zou, H., Wang, J.-S., et al., 2007b. Local plasma processes and enhanced electron densities in the lower ionosphere in magnetic cusp regions on Mars. *Planet. Space Sci.* 55, 2164–2172. doi:10.1016/j.pss.2007.07.003.
- Nielsen, E., H. Zou, D. A. Gurnett, et al. 2006. Observations of vertical reflections from the topside Martian ionosphere. *Space Sci. Rev.* 126, 373-388. doi: 10.1007/s11214-006-9113-y
- Němec, F., D. D. Morgan, D. A. Gurnett, et al., 2010. Nightside ionosphere of Mars: Radar soundings by the Mars Express spacecraft. *J. Geophys. Res.* 115, E12009, doi:10.1029/2010JE003663.
- Němec, F., D. D. Morgan, D. A. Gurnett, et al., 2011. Dayside ionosphere of Mars: Empirical model based on data from the MARSIS instrument. *J. Geophys. Res.* 116, E07003, doi:10.1029/2010JE003789.
- Picardi, G., Biccari, D., Seu, R., et al., 2004. MARSIS: Mars advanced radar for subsurface and ionosphere sounding. In: Wilson, A. (Ed.), *Mars Express: A European Mission to The Red Planet*, SP-1240. European Space Agency Publication Division, Noordwijk, the Netherlands, pp. 51–70.
- Rishbeth, H., Garriott, O.K. 1969. *Introduction to Ionospheric Physics*. Academic Press, New York.
- Safaenili, A., Kofman, W., Mouginot, et al., 2007. Estimation of the total electron content of the Martian ionosphere using radar sounder surface echoes. *Geophys. Res. Lett.* 34, L23204. doi:10.1029/2007GL032154, 2007.
- Shinagawa, H., 2000. Our current understanding of the ionosphere of Mars. *Adv. Space Res.* 26(10), 1599-1608.
- Smith, M. D., 2004. Interannual variability in TES atmospheric observations of Mars during

- 1999–2003. *Icarus* 167, 148–165. doi:10.1016/j.icarus.2003.09.010.
- Titheridge, J. E., 1998. The real height analysis of ionograms: A generalized formulation. *Radio Sci.* 23(5), 831-849
- Tyler, G. L., G. Balmini, D. P. Hinson, et al., 2001. Radio science observations with Mars Global Surveyor: Orbit insertion through one Mars year in mapping orbit. *J. Geophys. Res.*, 106, 327– 348.
- Wang, J.-S., and E. Nielsen, 2003a. Wavelike structures in the Martian topside ionosphere observed by Mars Global Surveyor. *J. Geophys. Res.* 108(E7), 5078, doi:10.1029/2003JE002078.
- Wang, J. S., and E. Nielsen, 2003b. Behavior of the Martian dayside electron density peak during global dust storms. *Planet. Space Sci.* 51, 329–338. doi:10.1016/S0032-0633(03)00015-1.
- Wang, J.-S., E. Nielsen, 2004. Evidence for topographic effects on the Martian ionosphere. *Planet. Space Sci.* 52, 881–886. doi:10.1016/j.pss.2004.01.008.
- Wang, X.-D. J.-S. Wang, E. Nielsen, H. Zou, 2009. “Hook” structure in MARSIS ionogram and its interpretation. *Geophys. Res. Lett.* 36, L13103, doi:10.1029/2009GL038844.
- Withers, P., 2009. A review of observed variability in the dayside ionosphere of Mars. *Adv. Space Res.* 44, 277–307. doi:10.1016/j.asr.2009.04.027.
- Withers, P., M. Mendillo, H. Rishbeth, et al., 2005. Ionospheric characteristics above Martian crustal magnetic anomalies. *Geophys. Res. Lett.* 32, L16204.
- Withers, P., M. Mendillo, 2005. Response of peak electron densities in the martian ionosphere to day-to-day changes in solar flux due to solar rotation. *Planet. Space Sci.* 53, 1401-1418. doi:10.1016/j.pss.2005.07.010.
- Zou, H., J.-S. Wang, and E. Nielsen, 2005. Effect of the seasonal variations in the lower atmosphere on the altitude of the ionospheric main peak at Mars. *J. Geophys. Res.* 110, A09311, doi:10.1029/2004JA010963.

Figure Captions

Fig. 1. Density plot showing the spatial distribution of the selected frames.

Fig. 2. An example of the selected ionograms for data extraction. The red crosses indicate extracted data points; the red vertical bar indicates the maximum plasma frequency extracted. The red arrow indicates the data point (f_1, τ_1) at which the density profile is partitioned into two parts during the inversion. The white curve is a simulated vertical echo trace using the inverted ionosphere parameters (the inversion method is explained in Sec. 3.2).

Fig. 3. Two examples of ionograms showing discernable echoes from the topside layers. (a) The echo trace from the first top layer is quite clear; (b) the echo trace from the first top layer is discernable, but diffuse and incomplete.

Fig. 4. A sketch indicating the simplification of the plasma density profile for inversion (see Sec. 3.2.2 for further explanation).

Fig. 5. Inverted solutions (z_m, H) for the ionogram shown in Fig. 2 based on the simplified model (Fig. 4). The crosses indicate optimal solutions found using 2 measurements (a) and 5 measurements (b).

Fig. 6. Occurrence frequency distribution of total fit (Q, a) and the composite correlation coefficient (R, b) for the 4988 inversions. The two panels share the same vertical coordinate.

Fig. 7. Density plots of peak density (N_m, a) , density peak height (z_m, b) and the neutral scale height (H, c) against the solar zenith angle (SZA) for all data. In each panel, the mean value (solid curve) and standard deviation (dashed curves) are calculated in 1° SZA bins. The

scatter point density (color bar) is calculated in $0.1^\circ \text{ SZA} \times 0.06\text{e}+10 \text{ m}^{-3} N_m$ intervals for panel a, $0.1^\circ \text{ SZA} \times 0.80 \text{ km } z_m$ intervals for panel b, and $0.1^\circ \text{ SZA} \times 0.20 \text{ km } H$ intervals for panel c. In panel c, ~ 100 extreme values of H (3.2 and 23.5 km) occur, which indicates unphysical inversions due to the ill-conditionedness of Eq. 10.

Fig. 8. Density plots of peak density (N_m , a), density peak height (z_m , b) and the neutral scale height (H , c) against Mars solar longitude (L_S) for all of the data. In each panel, the mean value (solid curve) and standard deviation (dashed curves) are calculated in $30^\circ L_S$ bins. The density of the scatter points (color bar) is calculated in $3^\circ L_S \times 0.06\text{e}+10 \text{ m}^{-3}$ intervals for panel a, $3^\circ L_S \times 0.80 \text{ km}$ intervals for panel b, and $3^\circ L_S \times 0.20 \text{ km } H$ intervals for panel c. In panel c, ~ 100 extreme values of H (3.2 and 23.5 km) occur, which indicate unphysical inversions due to the ill-conditionedness of Eq. 10.

Fig. 9. Scatterplot of the density of the supposed homogenous slab (N_{top}) against the top layer peak density (N_1) for all of the data. The mean value (solid curve) and standard deviation (dashed curve) of N_{top} are calculated in $0.1 \times 10^{10} \text{ m}^{-3} N_1$ bins. The color bar indicates the spacecraft altitude (z_{SC} , in 100 km) corresponding to each data point.

Fig. 10. Density plot of N_1 (a) and z_1 (b) against SZA. The mean value (solid curve) and standard deviation (dashed curve) are calculated in 1° SZA bins. The density of the scatter points (color bar) is calculated in $0.02 \times 10^{10} \text{ m}^{-3} N_1 \times 0.1^\circ \text{ SZA}$ intervals for panel a and in $0.1^\circ \text{ SZA} \times 2 \text{ km } z_1$ intervals for panel b.

Fig. 11. Density plot of N_1 (a) and z_1 (b) against L_S . In each panel, the mean value (solid curve) and standard deviation (dashed curves) are calculated in $30^\circ L_S$ bins. The density of the scatter points (color bar) is calculated in $0.02 \times 10^{10} \text{ m}^{-3} N_1 \times 3^\circ L_S$ intervals for panel a and in $3^\circ L_S \times$

1 km z_1 intervals for panel b.

Fig. 12. Density plot of N_1 against N_m . The mean value (solid curve) and standard deviation (dashed curve) of N_1 are calculated in $0.02 \times 10^{10} \text{ m}^{-3} N_m$ bins. The density of the scatter points (color bar) is calculated in $0.02 \times 10^{10} \text{ m}^{-3} N_1 \times 0.05 \times 10^{10} \text{ m}^{-3} N_m$ intervals.

Fig. 13. Scatterplot of z_1 against z_m for all of the data. The mean value (solid curve) and standard deviation (dashed curve) of z_1 are calculated in 7 km z_m bins. The color bar indicates the value of H (km) corresponding to each data point.

Fig. 14. Occurrence frequency distribution of the height difference ($z_1 - z_m$) (a) and the height difference normalized by the neutral scale height ($(z_1 - z_m)/H$) (b).

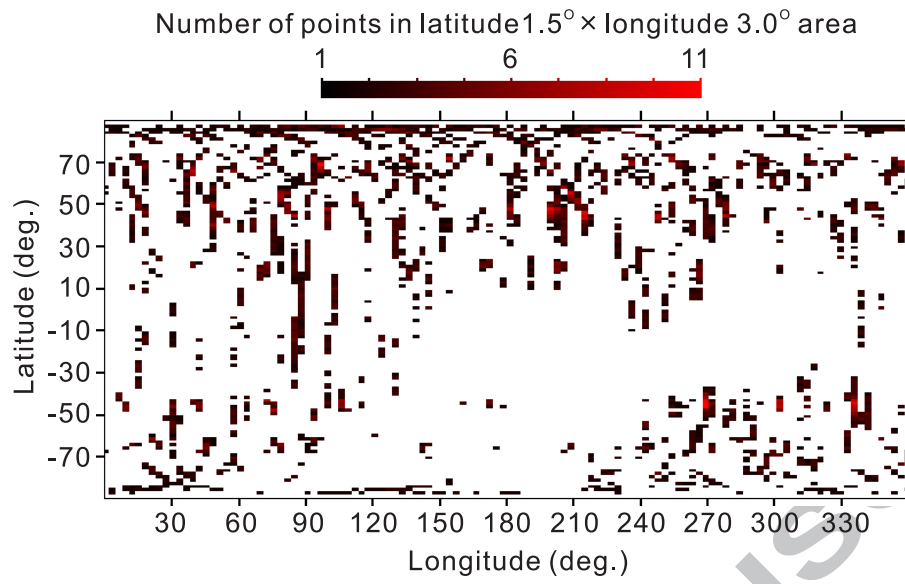
Fig. 15. Density plot of the height difference ($z_1 - z_m$) against H . The mean value (solid curve) and standard deviation (dashed curves) of ($z_1 - z_m$) are calculated in 2 km H bins. The density of the scatter points (color bar) is calculated in 1 km ($z_1 - z_m$) \times 0.2 km H intervals.

Fig. 16. Scatter plot of N_m (a) and N_1 (b) against the in situ cyclotron frequency. The color bar represents the spacecraft altitude corresponding to each of the data points in both panels. There are 1057 data points in each panel.

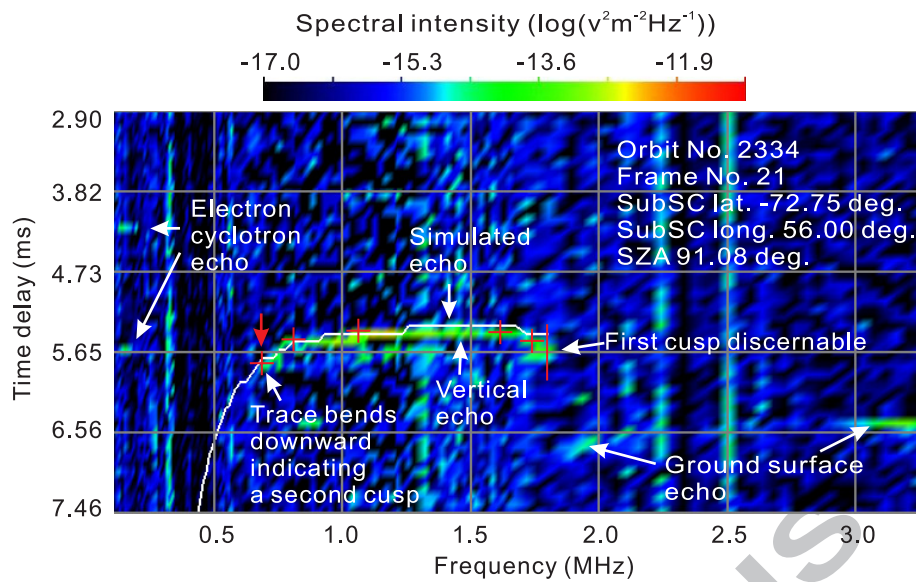
Fig. 17. Three examples of MGS RS ionospheric density profiles with notable “topside layers”. The arrows indicate the positions of the notable density peaks on the topside of the

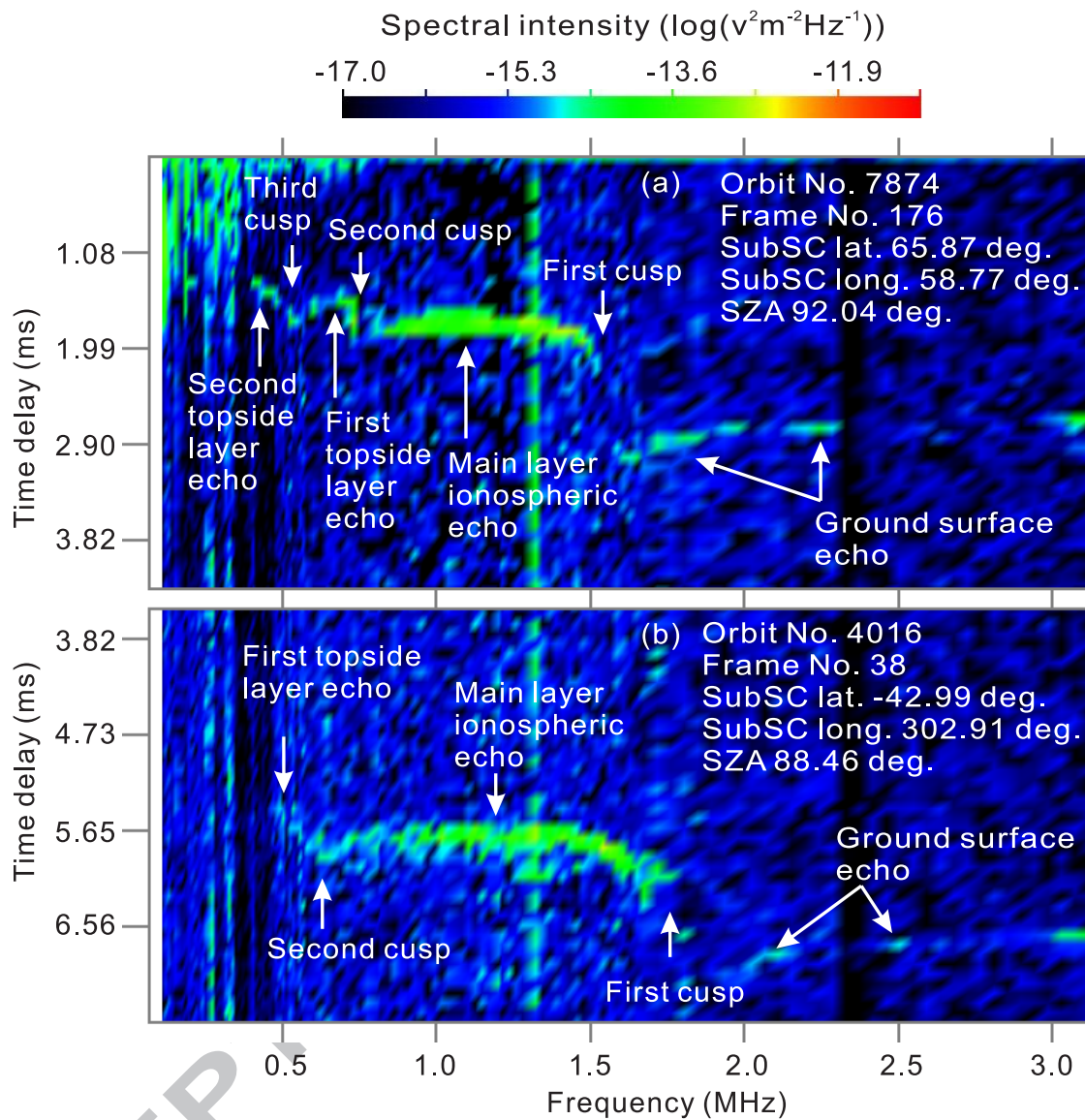
main layer; the bars indicate height positions equivalent to z_1 ; the height difference of an arrow-and-bar pair is indicated by " Δz_1 ". Details of the three profiles are as follows: (1) Data file 0315h13a.eds, orbit No. 7493, acquisition time 2000-11-10T06:57:41.881, SZA 85.65°, latitude 64.10°, longitude 34.41°. (2) Data file 0307u44a.eds, orbit No. 7402, acq. time 2000-11-02T20:28:50.421, SZA 86.42°, lat. 63.51°, long. 120.75°. (3) Data file 5155e22a.eds, orbit No. 27881, acq. time 2005-06-04T04:17:16.316, SZA 87.79°, lat. 65.00°, long. 102.87°.

ACCEPTED MANUSCRIPT

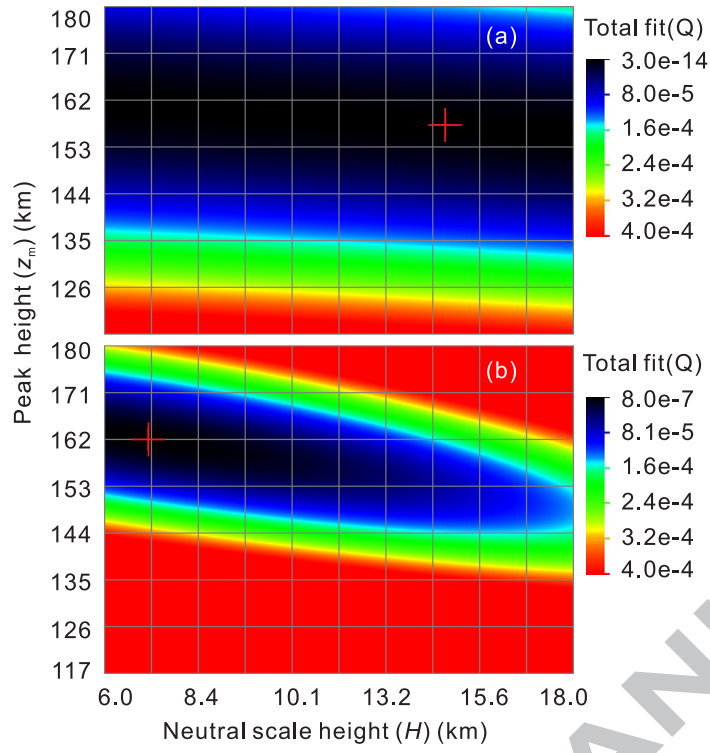


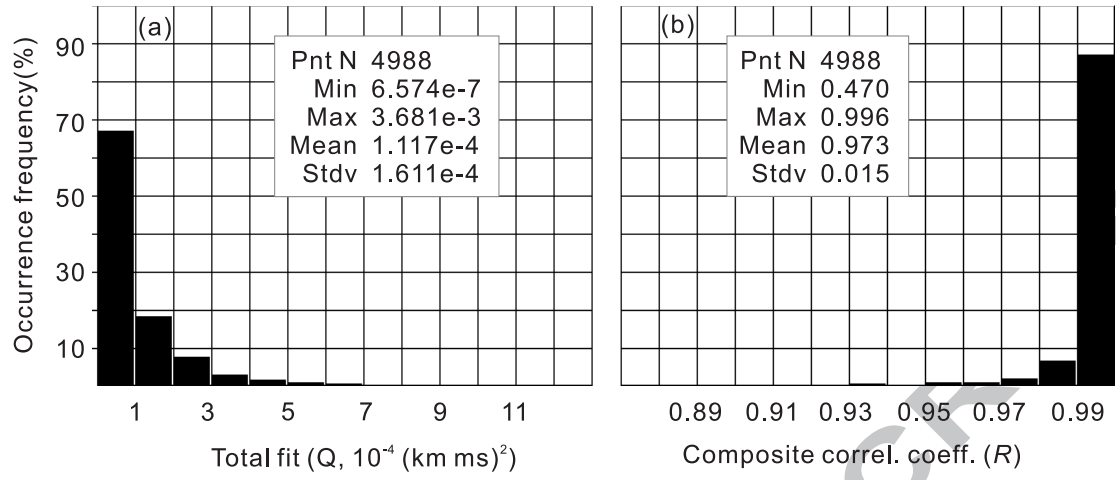
ACCEPTED MANUSCRIPT

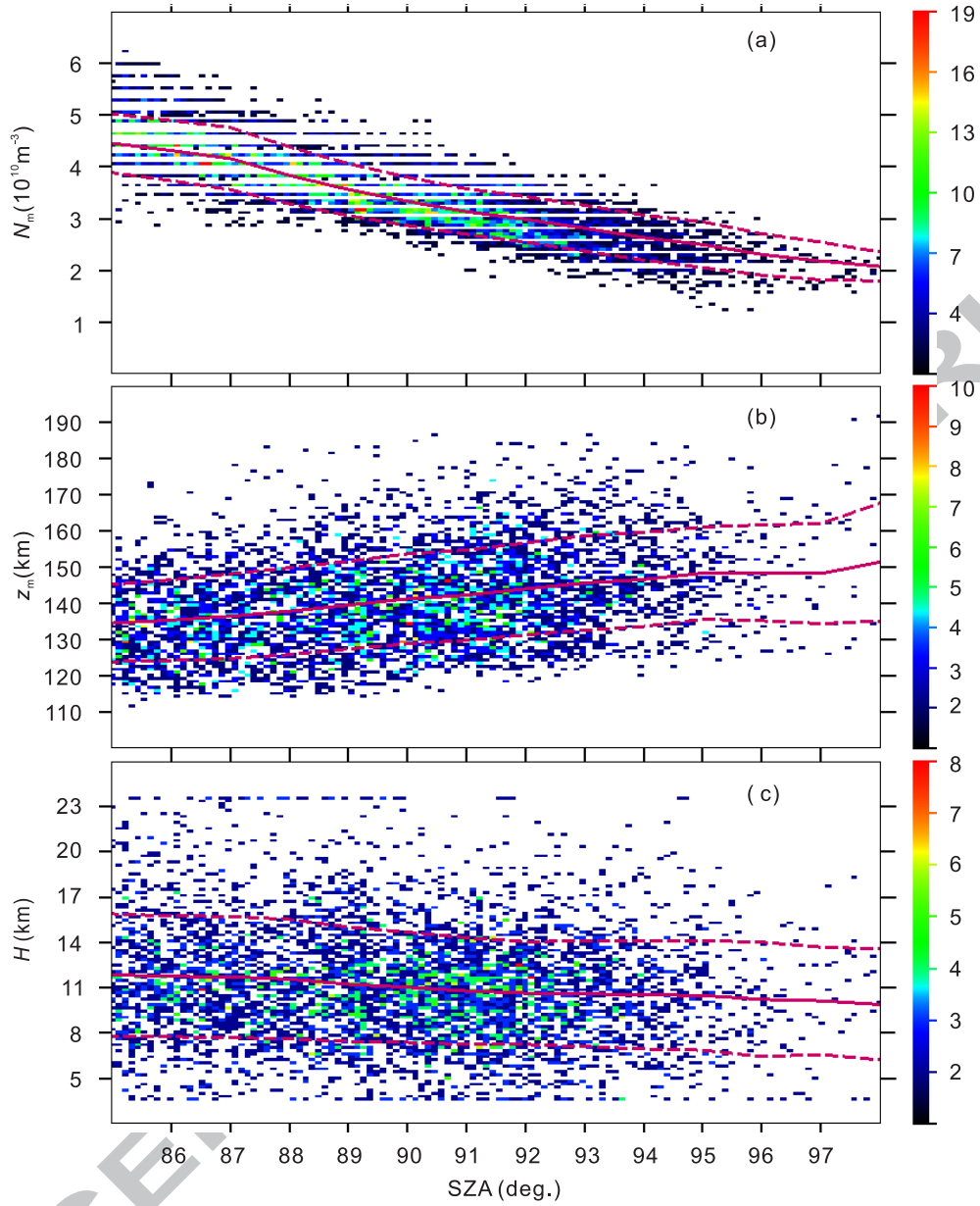


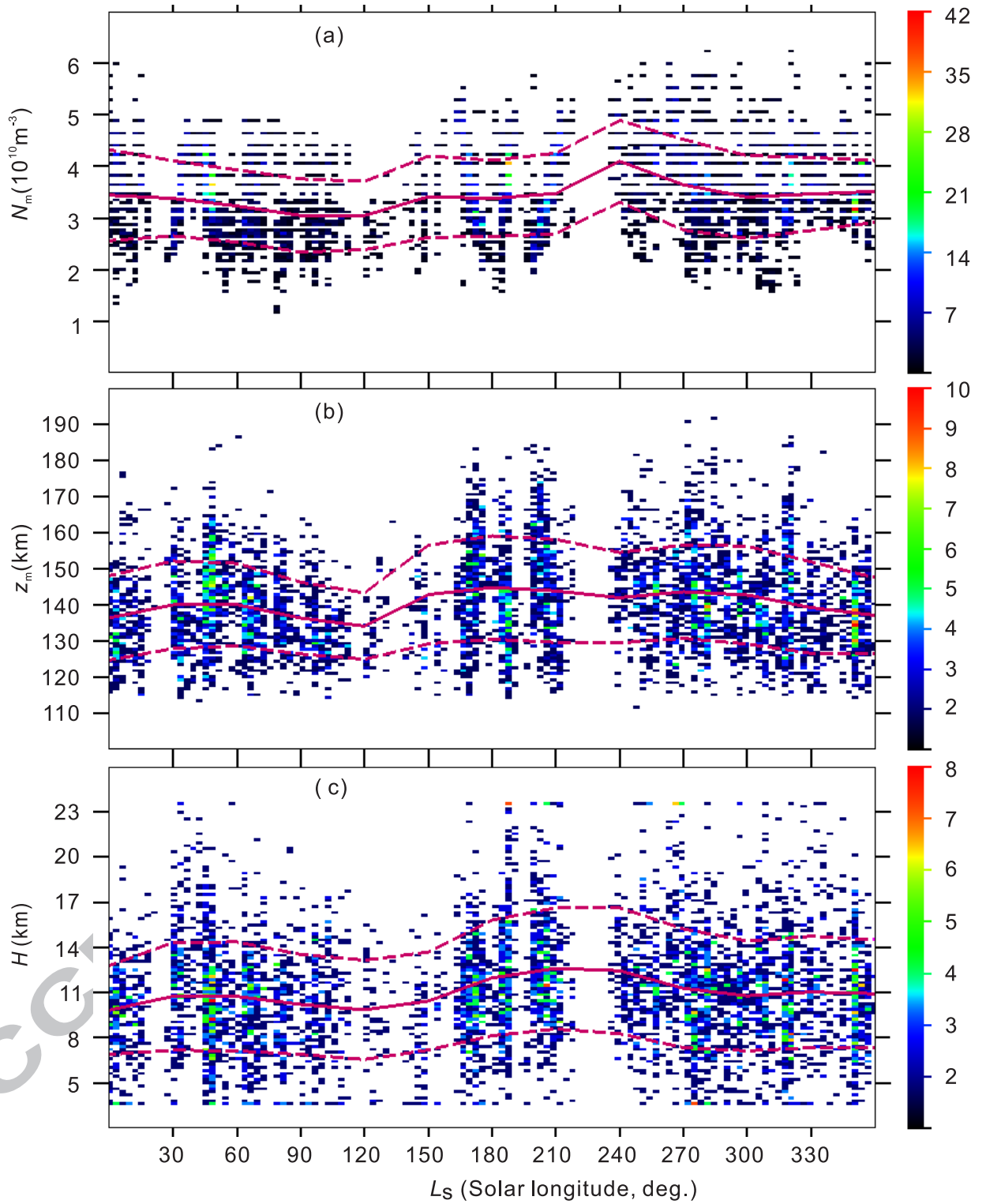


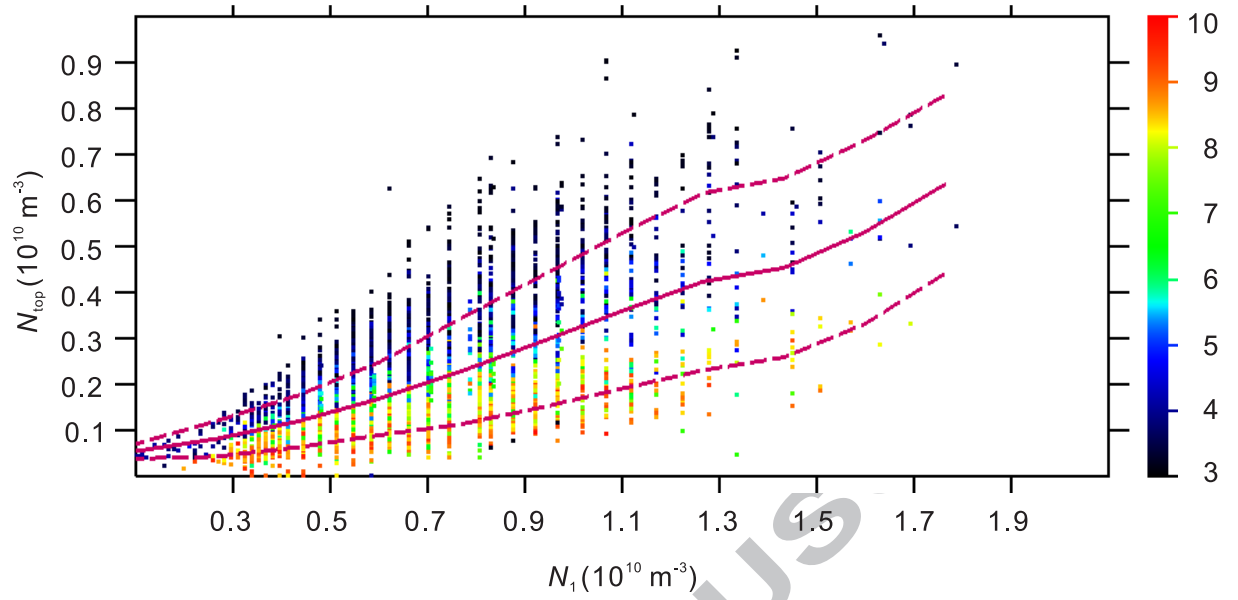
ACCEPTED

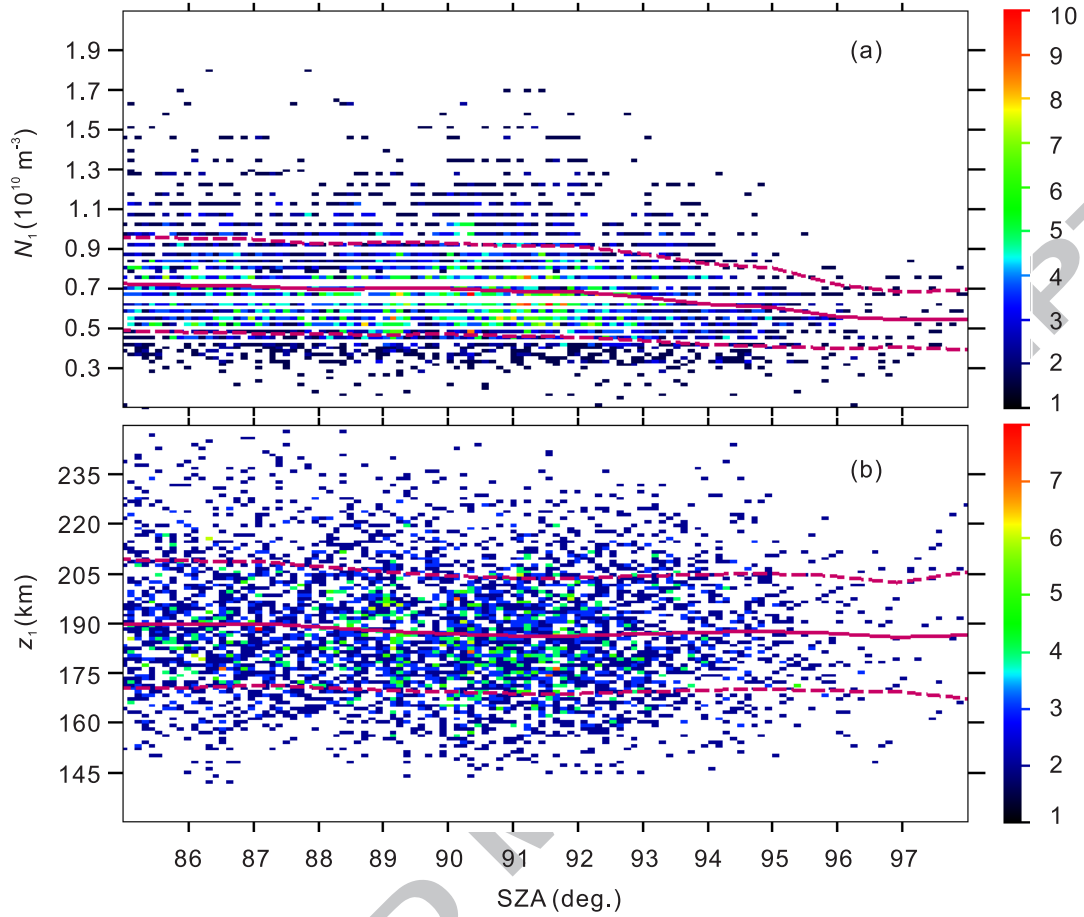


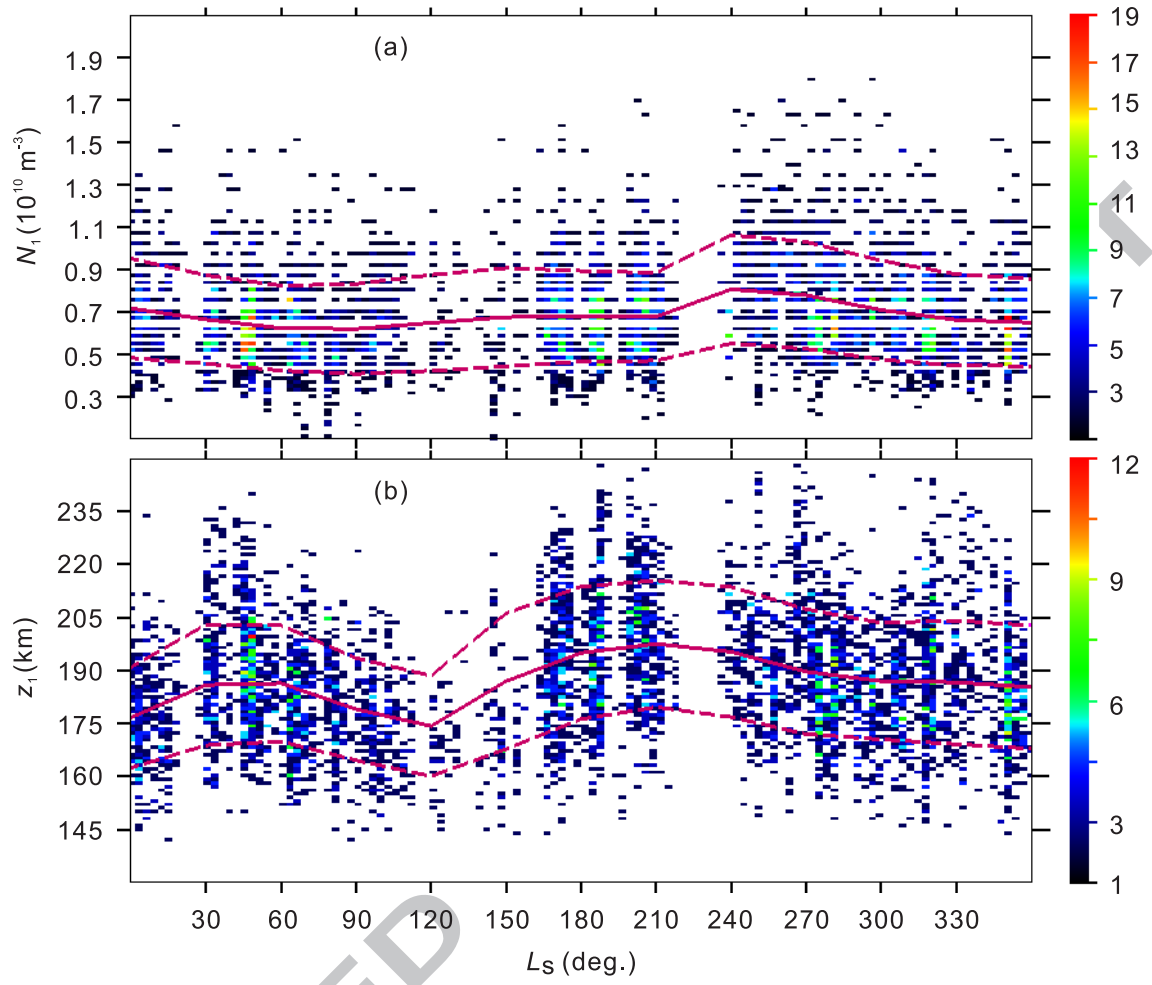


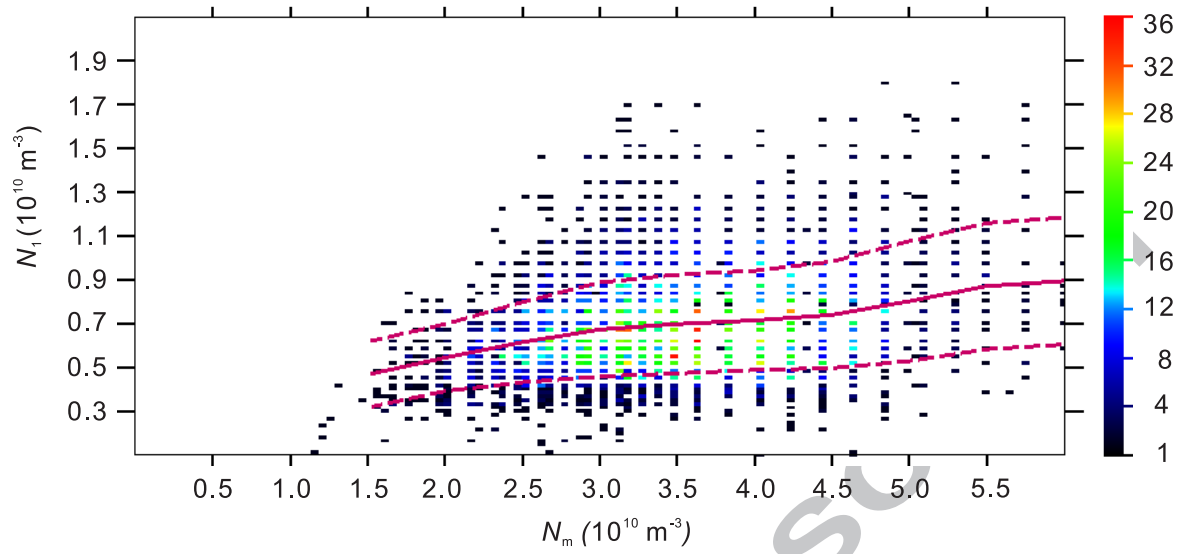


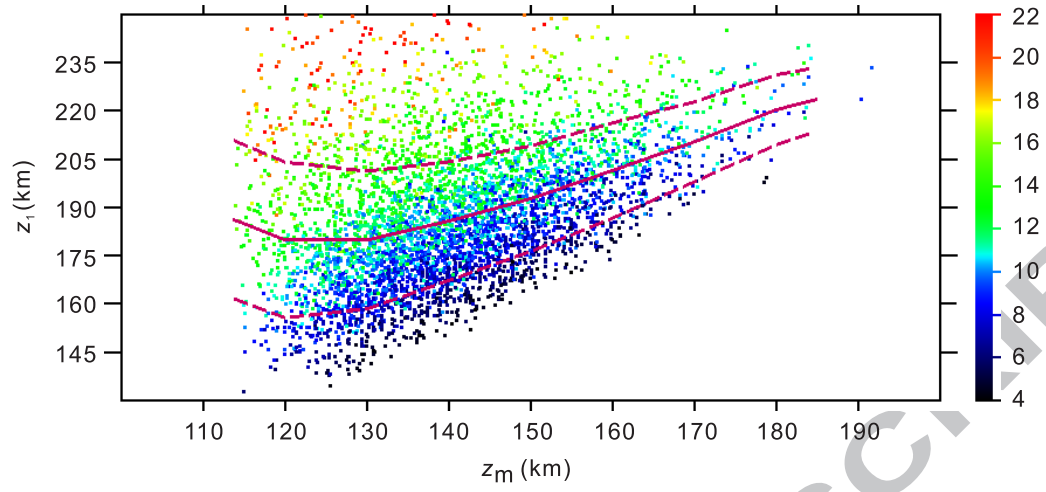


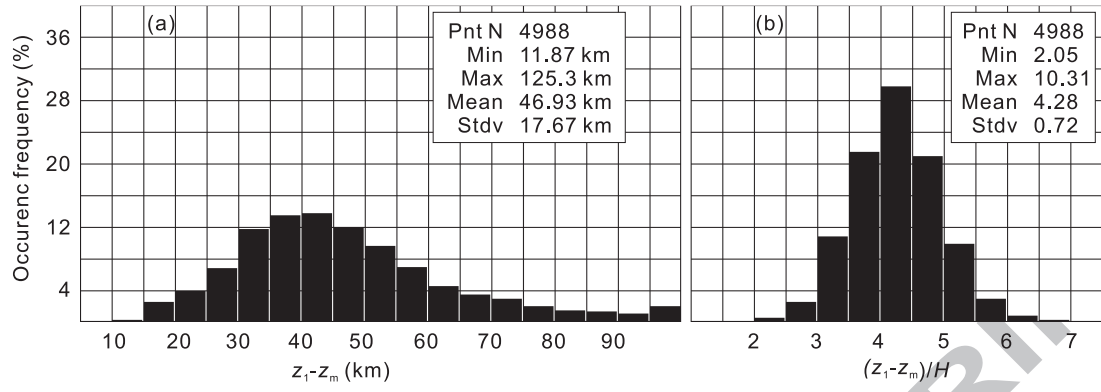




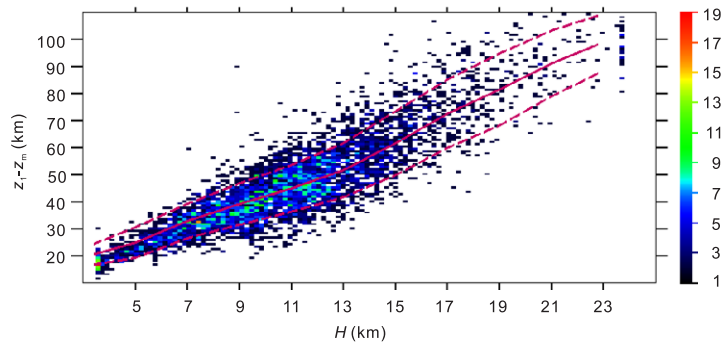




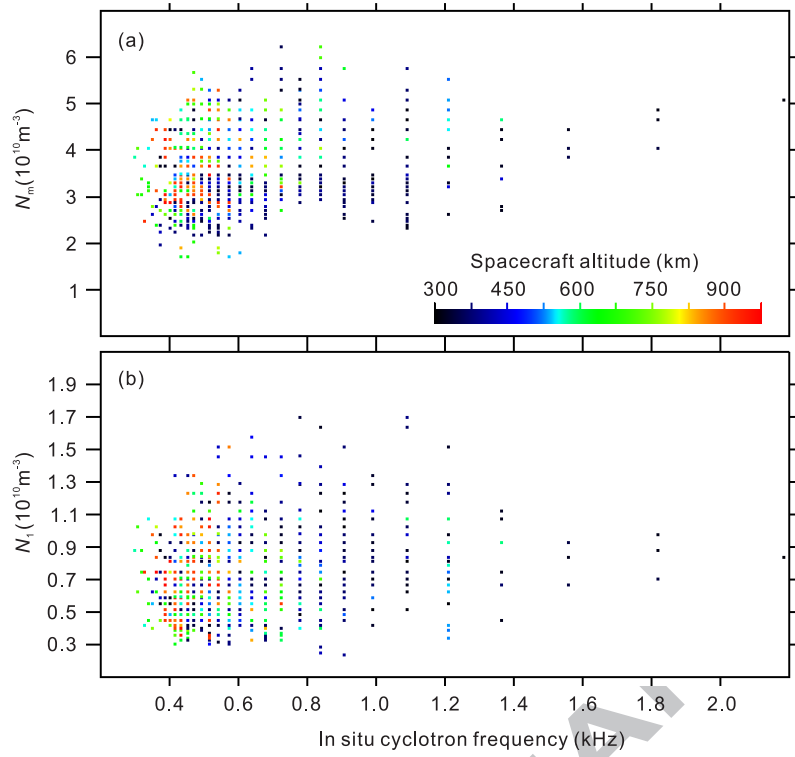




ACCEPTED MANUSCRIPT



ACCEPTED MANUSCRIPT



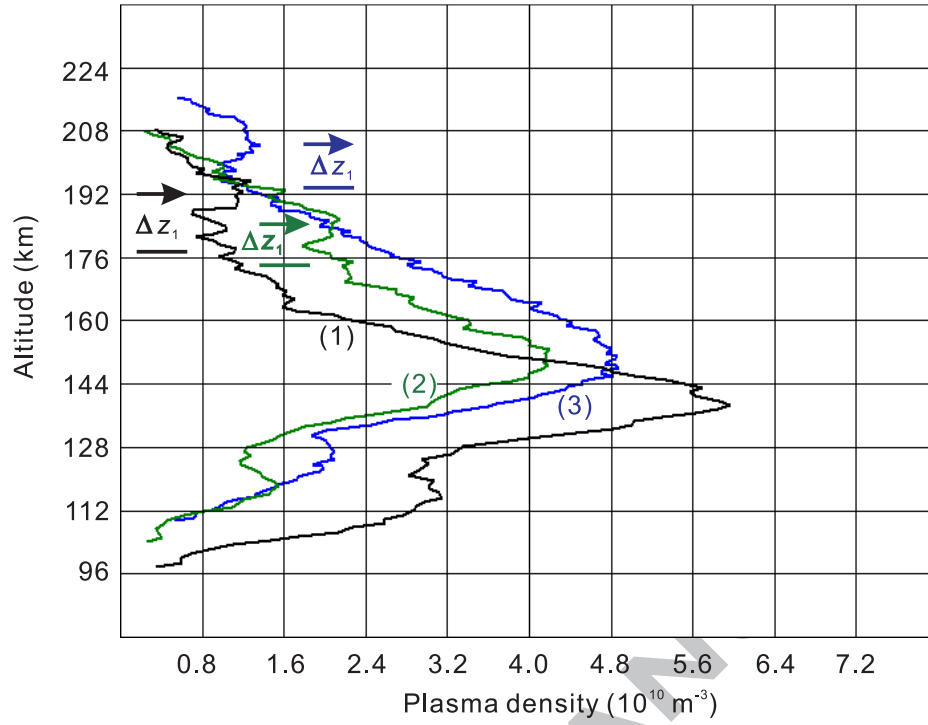


Table 1. Statistics of N_m , z_m and H at SZA=85° and 95°

	N_m (10^{10} m^{-3})		z_m (km)		H (km)	
	$\geq 85, < 86$	95 ± 1	$\geq 85, < 86$	95 ± 1	$\geq 85, < 86$	95 ± 1
SZA(°)						
Point number	449	298	449	298	449	298
Average value	4.65	2.36	134.30	148.07	11.91	10.27
Standard deviation	0.56	0.41	10.76	12.57	4.05	3.79
<i>Hantsch and Bauer, 1990</i> ^a			120–180		8.9–10	
<i>Fox and Yeager, 2006</i> ^b	4.4		149			
<i>Morgan et al., 2008</i> ^c	3.0 – 5.0		120–180		11 – 17	
<i>Withers, 2009</i> ^d					5 – 15	
<i>Němec et al., 2011</i> ^e	4 – 7	~2	120–180		10–25	

^a Mariner and Viking data.

^b Predictions using photoionization and electron impact models.

^c MARSIS data and inversion.

^d Synthetic result.

^e MARSIS data and inversion.

Table 2. Statistics of N_m , z_m and H for L_S ranges where data are dense

parameter	L_S (°)	Northern season	Point number	Mean value	Standard deviation
N_m (10^{10} m^{-3})	60 – 100	Summer	568	3.05	0.73
	240 – 280	Winter	668	3.81	0.89
z_m (km)	60 – 100	Summer	568	137.23	10.12
	240 – 280	Winter	668	144.48	13.31
	0(360)±20	Autumn	648	136.59	10.66
	170- 200	Spring	552	144.94	14.00
H (km)	60 – 100	Summer	568	10.13	3.27
	240 – 280	Winter	668	11.64	4.17
	0(360)±20	Autumn	648	10.28	3.15
	170- 200	Spring	552	11.91	4.06

Table 3. Statistics of N_1 and z_1 for L_S ranges where data are dense

parameter	L_S (°)	Northern season	Point number	Mean value	Standard deviation
N_1 (10^{10} m^{-3})	60 – 100	Summer	568	0.60	0.21
	240 – 280	Winter	668	0.81	0.28
z_1 (km)	60 – 100	Summer	568	180.13	14.44
	240 – 280	Winter	668	192.62	18.90
	0(360) \pm 20	Autumn	648	180.15	15.31
	170- 200	Spring	552	195.01	19.42

Highlights

We develop a MARSIS data inversion method applicable where echoes are unclear.

The topside transient layers resemble the main layer regarding seasonal variation.

The topside transient layers tend to occur ~60 km above the main density peak.

The topside transient layers become higher by ~10 km in the southern spring.

The topside transient layers are possibly formed by beam-plasma instabilities.

ACCEPTED MANUSCRIPT